

JA/IN/26/ENMF
2001 093 581

533 403
607

The Effect of Ballistic Impacts on the High Cycle Fatigue Properties of Ti-48Al-2Nb-2Cr (at.%)

S. L. Draper, B. A. Lerch, J. M. Pereira, M. V. Nathal, C. M. Austin*, and O. Erdman*

NASA Glenn Research Center at Lewis Field

Cleveland, OH 44135

*General Electric Aircraft Engines

Cincinnati, OH 45215

Abstract

The ability of γ - TiAl to withstand potential foreign and/or domestic object damage is a technical risk to the implementation of γ - TiAl in low pressure turbine (LPT) blade applications. The overall purpose of the present study was to determine the influence of ballistic impact damage on the high cycle fatigue strength of γ - TiAl simulated LPT blades. Impact and specimen variables included ballistic impact energy, projectile hardness, impact temperature, impact location, and leading edge thickness. The level of damage induced by the ballistic impacting was studied and quantified on both the impact (front) and backside of the specimens. Multiple linear regression was used to model the cracking and fatigue response as a function of the impact variables. Of the impact variables studied, impact energy had the largest influence on the response of γ - TiAl to ballistic impacting. Backside crack length was the best predictor of remnant fatigue strength for low energy impacts (<0.74J) whereas Hertzian crack length (impact side damage) was the best predictor for higher energy impacts. The impacted γ - TiAl samples

displayed a classical mean stress dependence on the fatigue strength. For the fatigue design stresses of a 6th stage LPT blade in a GE90 engine, a Ti-48Al-2Nb-2Cr LPT blade would survive an impact of normal service conditions.

I. Introduction

A joint program between NASA – GRC and GE Aircraft engines has been underway, with the aim of developing a design and manufacturing capability that will lead to engine test demonstration and eventual implementation of a Ti-48Al-2Nb-2Cr low pressure turbine (LPT) blade into commercial service. A low pressure turbine blade of a high-bypass turbofan engine presents the greatest weight savings potential for γ - TiAl. The temperatures are suitable for this material in the last two stages and the strength requirements are modest. In addition, catastrophic failure of blades in these stages would have a relatively minimal impact on engine performance and safety. Thus, design confidence in this material can be gained with minimal risk. One of the goals of the program was to realize a weight savings of 70 kg per stage (40% weight reduction from currently used Ni-base superalloys) while maintaining the current system cost. One of the technical risks of implementing γ - TiAl into service is its poor impact resistance in comparison to currently-used nickel-based superalloy, Rene 77. Due to the location in the engine, domestic object damage (DOD) is more likely to occur than foreign object damage (FOD). Engine test hardware were examined and service shop personnel surveyed to determine the severity and frequency of DOD on these blades such that a typical impact event could be defined. The conclusion was that “impact damage does not occur in LPT blades, absent a significant upstream event” [1]. However, due to the lower capabilities of γ - TiAl with respect to impact damage, the

fatigue capability of gamma airfoils with impact damage needed to be defined for risk abatement.

The overall objective of the current work was to determine the influence of ballistic impact damage on the high cycle fatigue (HCF) life of γ - TiAl simulated LPT blades, as HCF is the probable failure mechanism of impacted LPT blades. An effort was made to capture as much of actual engine conditions as possible in laboratory tests. This included a cast, flat γ -TiAl test specimen whose edges simulated the leading edge of a LPT blade. The study was carried out in four phases.

II. Approach

Phase I was designed to study the effect of specimen thickness and impact energy on the fatigue strength of TiAl. Unfortunately, the specimens contained porosity in the center of the gage section and were unsuitable for fatigue testing. However, the leading edges were dense and adequate for studying the cracking characteristics of the material after impacting. The results are included in combination with the results from other phases of the investigation later in the paper. For Phase I, projectiles with 3.2 mm diameter were used because this was the only size the impact rig could accommodate at the beginning of the program. Additionally, impact trials were performed on cast Rene 77 impact specimens with the 3.2 mm projectiles at 174 m/s (2.0 J). The impacts produced dents but no cracks on the Rene 77 material and therefore, the 3.2 mm projectiles were thought to be suitable. The velocity was varied such that the energy ranged from 0.33 – 2.0 J. The resulting impacts on γ -TiAl were larger than desired and after an analysis of probable impact events, engine conditions, and debris collected during engine tests, a decision

was made to modify the gun barrel to accommodate smaller projectiles, 1.6 mm in diameter, for Phase II.

Phase II was a design of experiments (DOE) approach which was planned and implemented to study the microstructural features of TiAl after impacting, utilizing the porosity-containing samples. In this way, several of the impact variables could be eliminated and the number of HCF tests required in phases III and IV would be minimized. The variables selected for study included the energy of impact (E), thickness of specimen leading edge (t), and hardness of projectile (H). The temperature of impact (T) was selected as a variable for a side experiment. The design of experiments for Phases I and II are shown in Figure 1. The energy range was selected based on the velocity ranges and angles of incidence expected for particles in the LPT section. Damage at the last two stages of the LPT would most likely come from domestic objects, i.e. pieces of honeycomb seals, coatings, or pieces of Ni-base superalloys. The hardness of these materials at the operating temperature of an engine would not be as high as that of a steel bearing (the projectile used in these experiments). Therefore, half of the steel projectiles were annealed at 700°C for 1 hour to soften them to a hardness of approximately 20 HRC and projectile hardness was included as a variable. Specimens with three different thicknesses and bluntness of the leading edge were selected which simulated possible leading edge configurations for a low pressure turbine blade. The effect of impact temperature on the impact resistance of TiAl was studied in a side experiment.

The results of Phase II revealed that LPT blades should be as thick as possible for improved impact resistance and that impact energy is the most important determinant for crack

size. Therefore, only thick specimens were cast for the phase III and IV fatigue studies and the impact variables were down-selected to only energy. The objective for Phase III was to estimate the residual fatigue life after impacting at various energy levels, including energy levels higher than expected for impacts in service. Impact energy was varied from 0.20 to 1.55 J using both 1.6 and 3.2 mm annealed steel ball-bearing projectiles. The objective of Phase IV was to determine the effect of tensile mean stress on the fatigue life of impacted Ti-48Al-2Nb-2Cr. Two impact energies, 0.71 and 1.52 J, were selected and impacted specimens were fatigued at three different loading ratios. Based on Phase III, the 0.71 J impact represents an impact event in which the LPT blade still meets the formal required fatigue strength (includes a safety factor), whereas the 1.52 J impact represents the worst impact that a LPT blade could experience and not fail during service.

III. Materials and Procedures

Impact specimens were cast to size, in a dog-bone configuration, by Precision Castparts Corp. (Portland, OR). The flat specimens had a double-reduced gauge section, that was elliptical in cross-section and 25 mm wide. The edges simulated leading edges of actual LPT airfoils, Figure 2. The samples were processed in a sequence typical for a low pressure turbine blade. Hot isostatic pressing, chem-milling, heat treating, and media finishing were followed by an exposure at 650 °C for 20 hr to simulate typical embrittlement at service conditions. Two different batches of specimens were used in this study. The first batch was used in the microstructural DOE study and contained specimens with three different leading edge thicknesses, each with a different bluntness. The specimen thicknesses in the center of the gage

sections were 2.1, 2.6, and 3.7 mm. The thin specimen geometry simulated the currently used Rene 77 blades while the thicker geometries were configured in anticipation of the poorer performance of TiAl in ballistic impact resistance compared to superalloys. The second batch of specimens was cast using only the thickest geometry and these specimens were used for the fatigue studies.

The microstructure of the specimens was studied using polarized light on an optical microscope. Grain size was measured using a line intercept technique and lamellar volume fraction was determined through point counting. All error estimates represent 95 pct confidence intervals (C.I.) assuming a Gaussian distribution. The Al content of the samples was determined by x-ray fluorescence (XRF) while the remaining elements were analyzed by inductively coupled plasma emission spectrometry (ICP) and gas analysis.

The ballistic impact rig consisted of a precision gun barrel mounted on a load frame with an attached furnace, Figure 3. Steel projectiles were accelerated down the gun barrel by the release of compressed helium. A laser device measured the velocity of the projectiles near the end of the gun barrel. The gun barrel, which was 4 mm away from the leading edge of the specimen, was at a 90° angle to the width of the specimen. The projectiles were either 1.6 or 3.2 mm diameter steel ball bearings with a mass (m) of 0.0164 and 0.131 g, respectively. The kinetic impact energy was calculated based on $E = \frac{1}{2} mv^2$. The projectiles had a hardness of approximately 60 HRC in the as-received condition and ≤ 20 HRC after annealing at 700 °C for 1 hr. The specimens were impacted while maintained under a tensile stress of 70 MPa, simulating

operating conditions for LPT blades. Except for the temperature side experiment, all impacts were done at 260 °C. This was believed to be the lowest temperature at which an impact event would occur in service. For the temperature side experiments, specimens were impacted at 23, 260, 650, or 982 °C. For Phase II, the microstructural analysis DOE, the specimens were impacted three times with one impact condition along one edge of the specimen. The sample was then flipped over and impacted three more times with a different impact condition. For Phases III and IV, specimens were impacted three times with the same conditions. Two impacts were placed on one edge of the sample separated by approximately 2 cm, and one additional impact was placed on the opposite edge, centered between the other two impacts and on the opposite face of the specimen (Fig. 2). It was hoped that by impacting at three locations along the leading edge, the effects of variability in local microstructure would be normalized from sample to sample and the scatter in fatigue data would be minimized. It will be shown in this paper that one impact would have sufficed for fatigue testing. However, a statistical distribution of damage was expected and the number of impacts examined microscopically could be increased using multiple impacts per sample. The nominal distance from the leading edge to the impact center (denoted X) was 0.51 mm for the small projectiles and 0.64 mm for the large projectiles but specimen variability and an imprecise fit between the projectile and gun barrel resulted in some deviation in the aimed distance.

Static mechanical properties of the materials used in Phases I-IV were measured using miniature tensile specimens machined by low stress grinding from the grip end of impact specimens selected from both castings. The 51 mm long specimens had a 19 mm gage length

and a 4 mm diameter. The tensile specimens were tested in air at room temperature and 650 °C using a constant strain rate of $1 \times 10^{-4} \text{ s}^{-1}$. Strain was measured with a 12.7 mm gage length axial extensometer attached to the gage of the specimen.

After impacting, the specimens were examined in a scanning electron microscope (SEM). Photographs used for measuring crack lengths were taken at 20 to 40X. Five types of crack lengths (Figure 4) were measured: 1) Front side major, 2) Front side total, 3) Hertzian, 4) Backside straight, and 5) Backside total. Front side major is a summation of the largest, somewhat continuous cracks observed on the front (impacted) side of the specimen while front side total is a summation of the length of all cracks observed. A Hertzian crack was defined as the longest crack on the impact side of the sample that was at an angle from the impact to the specimen edge, Figure 4. Backside straight is the length from the specimen edge to the end of any cracking on the backside of the impact, whereas backside total is a summation of all the crack lengths on the backside of the sample. Additionally, the distance from the center of the impact to the specimen edge (designated X in Fig. 4) was measured.

As-received and impacted samples were tested in high cycle fatigue at 650 °C with a frequency of 100 Hz. Fatigue crack growth rate is the highest at 650 °C for Ti-48Al-2Nb-2Cr [2] and therefore, this temperature was chosen for testing to simulate the worst case scenario. Phase III fatigue tests were all run with a load ratio, R , of 0.05 ($R = \sigma_{\min}/\sigma_{\max}$). Load-ratios of 0.05, 0.2, and 0.5 were used in Phase IV. Four fatigue tests were run for every impact condition/load-ratio combination. Due to the flat nature of γ -TiAl's S-N (stress vs. cycles to failure) curve, step

fatigue tests were used to determine the maximum fatigue strength after impacting[3,4]. Based on the impact condition and previous experience, a starting stress level was chosen. If the sample survived either 10^6 (Phase III) or 10^7 (Phase IV) cycles, the stress was increased by 6.9 to 13.8 MPa and run to failure or 10^6 or 10^7 cycles. The stress level was increased until failure (two pieces) occurred. Fatigue strength was taken as the stress at the next to last step, i.e., the stress representing the fatigue threshold. The use of step fatigue testing avoided wasting a large number of samples due to run-outs as each sample was forced to fail.

IV. Results

A. Chemistry and Microstructure - The γ -TiAl alloy used in this study was Ti-48Al-2Nb-2Cr, Table I. The Al level was determined by x-ray fluorescence using powder metallurgy TiAl standards that covered high and low aluminum levels. This technique has been shown to have better accuracy in determining the Al level in TiAl [1]. The Al level was slightly higher in the first batch of samples used in the microstructural analysis study than for the second batch used in the fatigue study, 48.0 vs. 47.5 at. %. The interstitial content was within the specification range for this alloy.

The microstructures of both castings were typical for Ti-48Al-2Nb-2Cr and consisted of equiaxed gamma grains and γ/α_2 lamellar regions, Figure 5. Casting 1 had a lower lamellar content, 0.20 ± 0.05 (95% C.I.) area fraction, compared to casting 2 which averaged 0.39 ± 0.06 . The grain size of casting 1 was statistically equivalent to the grain size of casting 2 and averaged $64.0 \pm 2.3 \mu\text{m}$ in transverse sections.

B. Tensile Properties

The tensile properties of both castings, Table II, are typical for this alloy [1]. The ultimate tensile strength (UTS), plastic elongation to failure (ϵ_p), and elastic modulus (E) were statistically equivalent between the two castings at both 23 and 650 °C as was the elevated temperature 0.2% yield strength (σ_y). Note that the confidence intervals for the 650 °C, casting #1 data are large due to the small number of successful tests (one sample failed on specimen loading). The 23 °C yield strength was statistically higher for the specimens from the second casting (lower Al content), although the difference between the two castings was still small. This was consistent with and attributed to the yield strength being inversely proportional to Al level for this alloy [1].

C. Effect of impact energy, projectile hardness, specimen thickness, and X on crack morphology (0-0.35J Energy Range, Phase II)

The type of impact damage produced depended on the specimen thickness as well as on the energy level of the projectile, Figures 6 and 7. Low energy impacts resulted in dents but very little cracking for both thin and thick specimens on the front side of the specimens. At higher energies, front side circumferential cracks, also termed “Hertzian” cracks, initiated at the impact crater and grew towards the specimen edge. These Hertzian cracks extended through the thickness of the specimen, producing an expanding half-cone shaped crack that resembles the Hertzian cracks commonly observed in glass [5]. For extreme conditions, this crack propagated completely through the specimen and resulted in a blow-out, i.e. a cone shaped chunk of material

was completely removed. An example of a nearly blown-out thin specimen is shown in Figure 7(a and c). The Hertzian cracks had nearly penetrated through the thickness and were visible from the backside of the sample. Simultaneous with this front side cracking, a straight crack was produced on the backside of the specimen, opposite to the impact. This cracking usually proceeded from the specimen edge to roughly the location opposite the impact crater. These backside cracks were perpendicular to the loading axis of the fatigue specimen and occasionally branched out in several directions as shown in 7c. At low energies, backside cracks were only observed with the thin and medium thickness specimens, Figure 6. Backside crack lengths increased with increasing impact energy. For blow-outs, the backside crack length was measured from the edge of the sample to the backside of the hertzian crack, Figure 7c.

The backside straight crack length was plotted as a function of energy in Figure 8. The backside straight crack length was strongly dependent on the projectile energy but the projectile hardness had no effect on backside straight crack length or any of the other crack type measured. Therefore, unless otherwise stated, the hard and soft projectile data were pooled. The thin (t1) and medium thickness (t2) specimens exhibited similar crack resistance for the low and medium energies while the backside straight crack length increased substantially for the thin specimens impacted at high energies as these specimens were either blow-outs or near blow-outs. The thin and medium thickness specimens also exhibited cracking at very low energy levels, whereas the thick specimens could withstand some level of impact without cracking. In general, the thick specimens exhibited improved impact resistance for the energy levels used in Phase II and this led to the selection of the thicker specimens for the follow-on fatigue studies, as well as thicker leading edges for the LPT blades.

Multiple linear regression was used to model the cracking and fatigue response as a function of impact variables. Included in the multiple regression models was X, the location of the center of the impact crater from the specimen edge, as variations in X could potentially result in large variations in cracking degree and ultimately fatigue life. The variables were normalized by subtracting the median value from the variable and dividing by half of the variable range. In this way, each term's coefficient indicates the relative importance of that term to the model. The models are only valid over the range studied for each variable. Full 2nd order models, including main, interactive, and quadratic terms were estimated for Phase II. Interactive terms, i.e. E*X, indicate that the effect of a variable is dependent on the level of another variable. Terms were included in the models at a significance level of 0.05 or lower. A summary of the models for all 5 crack types in Phase II is shown in Table III.

Of the main variables, energy, thickness, hardness, and X distance, energy was the most important for all crack types. Thickness was more important for the backside crack types but also had some significance for the front crack types. Projectile hardness did appear in two models but with small coefficients. X appeared in the models as a small main effect for two of the front crack types but was also included as an interactive term in several of the models and as a quadratic term for backside straight cracks. The occurrence of a blow-out (BO) was included in two of the models and was a major effect for the backside straight cracks, due to the method of measurement. The backside straight cracks were measured from the leading edge to the end of the blowout on the backside, Figure 7c, which is actually the backside of the Hertzian crack. The backside crack would have been smaller in length and contained in the blown-out portion. As Table III indicated, all of the various crack measurements can be accurately described as

functions of the impact parameters. Values for R^2 (sample correlation coefficient) in the 85-90% range indicate that most of the variability in crack lengths can be accounted for by these models.

The follow-on fatigue studies determined that the Hertzian and backside straight cracks were the most directly linked to fatigue failure, therefore, these two crack measurements are emphasized in the plots and discussion. A best fit for the Hertzian crack length (HCL) was obtained by square root transforming the response. The model for the Hertzian crack is given by:

$$HCL^{1/2} (mm^{1/2}) = 0.500 \frac{(E - 0.199)}{0.154} - 0.199 \frac{(t - 2.832)}{0.724} - 0.229 \frac{(X - 0.546)}{0.419} + 0.181 \frac{(t - 2.832)}{0.724} * \frac{(X - 0.546)}{0.419} - 0.174 \frac{(E - 0.199)}{0.154} * \frac{(X - 0.546)}{0.419} + 0.662; R^2 = 89 \% \quad (1)$$

where E is energy, t is thickness, and X is aiming distance. The variables are normalized such that their coefficients indicate their relative importance in the model. For example, energy was twice as influential to the length of the Hertzian cracks as any other variable. Interactive terms of thickness and X position were significant, as were energy and X. An example of E*X on Hertzian crack length for the three sample thickness is shown in Figure 9. This figure shows that X had little effect on Hertzian crack length for the thick specimens, but hitting closer to the leading edge of thin and medium thickness specimens resulted in a large increase in Hertzian crack length at high energies. Energy was more influential on Hertzian crack length when the sample was hit closer to the leading edge. The thickest samples had the shortest HCL's over the range of energy and X studied in Phase II, Figure 9c.

The regression model for backside straight crack length (BSCL) for Phase II is as follows:

$$\begin{aligned}
 BSCL(mm) = & 0.443 \left[\frac{(X - 0.546)}{0.419} \right]^2 + 0.447 \frac{(E - 0.199)}{0.154} - 0.365 \frac{(t - 2.832)}{0.724} + \\
 & 0.351[(BO = 1) \text{ or } (noBO = -1)] - 0.085 \frac{(H - 40)}{20} + 0.361 \frac{(t - 2.832)}{0.724} * \frac{(X - 0.546)}{0.419} \\
 & - 0.269 \frac{(E - 0.199)}{0.154} * \frac{(X - 0.546)}{0.419} + 0.065 \frac{(t - 2.832)}{0.724} * \frac{(H - 40)}{20} + 1.173; \quad R^2 = 91 \% \quad (2)
 \end{aligned}$$

where BO designates a blow-out and H is projectile hardness.

The majority of the impacts were not blown-out for Phase II, but the BO term was necessary to describe the jump in backside crack length that occurred for blown-out samples. Projectile hardness was included in the model as both a main effect and an interaction, however, the coefficients were small indicating a very minor effect. The set of three, one for each thickness, 3-D plots in Figure 10 illustrates the effect of E, X, and t on backside straight crack length for Phase II. For all thicknesses, the impact energy had a stronger effect on backside straight crack lengths (as with Hertzian cracks) when hitting close to the leading edge. The longest backside cracks occurred for thin specimens hit close to the leading edge with the largest impact energy.

The aim distance, X, was included as a variable in all but one of the Phase II crack length models, Table III, but usually as a minor effect. The accuracy of the aim for the 1.6 mm projectiles used in Phase II was fairly high. The target value of X was 0.51 mm but averaged slightly higher at 0.61 ± 0.28 mm with a range from 0 to 0.9 mm. The range in X values was

larger in Phases III and IV, and therefore the effect of X on both backside straight crack length and Hertzian crack length was more pronounced and will be discussed in later sections.

D. Effect of Impact Temperature

The effect of impact temperature on crack length was studied in a side experiment with temperature (T) and projectile hardness as the main variables. Energy and X position were kept as constant as possible but still varied, especially at room temperature, due to the nature of the test. The effect of temperature on the length of the front Hertzian cracks and the backside cracks is shown in the plots of Figure 11, however, the effect of the slight variations in energy and X are not taken into account in these plots. The Hertzian crack length decreased with increasing temperature. Backside crack lengths decreased from 23 °C to 650 °C and then increased at 1000 °C. Unfortunately, the X distance was larger than average for the 1000 °C data and the increase in BSCL could be attributed to the large X. The data were analyzed by multiple regression to incorporate energy, X, and projectile hardness, as well as temperature. Interactive terms were not allowed in the models because the variations in energy and X did not cover the design space and led to an unbalanced data set. The temperature side experiment models are given below:

$$HCL^{1/2} (mm^{1/2}) = -0.203 \left[\frac{(T - 502.5)}{479.5} \right]^2 + 0.246 \frac{(E - 0.176)}{0.031} - 0.238 \frac{(T - 502.5)}{479.5} - 0.138 \frac{(X - 0.733)}{0.261} + 0.367; \quad R^2 = 85 \% \quad (3)$$

$$BSCL (mm) = 0.411 \frac{(X - 0.733)}{0.261} - 0.195 \frac{(T - 502.5)}{479.5} + 0.129 \frac{(E - 0.176)}{0.031} - 0.089 \frac{(H - 40)}{20} + 0.602; \quad R^2 = 76 \% \quad (4)$$

The major factors in the Hertzian crack model were energy and temperature, with temperature having a negative coefficient (i.e., increasing temperature decreases crack length) and energy having a positive coefficient. X position and the square of temperature, both of which had negative coefficients, were also included. The backside straight crack length model had an R^2 of only 76. Intentionally varying energy and X along with temperature may result in a better model, as interactive terms could be included. Where X had a negative coefficient for Hertzian cracks, it had a positive coefficient for backside straight cracks, i.e. larger X's result in shorter Hertzian cracks but longer backside cracks. 3-D plots illustrating the models as a function of temperature, energy, and X are shown in Figure 12. Energy was held as constant as possible for the temperature side experiment and yet energy varied enough to significantly affect the crack lengths. Therefore, energy was modeled to have similar coefficients as temperature for both Hertzian and backside straight crack lengths.

E. Effect of impact energy and X on crack morphology (0 – 2.0 J Energy Range (Phases I-IV).

The overall objective of the follow-on studies was to determine the effect of impact damage on the fatigue strength of TiAl. However, crack lengths were measured on all impacted samples and the data were pooled with the data from previous phases for further analysis. Hertzian and backside straight crack lengths are plotted as a function of energy for all four phases in Figure 13. The level of impact damage was similar for both 1.6 and 3.2 mm projectiles when impacted at similar energies. However, there was more of a tendency for the thin specimens to be blown-out when impacted with the small projectiles. The smaller projectiles resulted in smaller diameter indents on the sample surface. Therefore, the smaller projectiles

caused a larger stress under the impact than did the large projectiles when impacted with the same energy. Unlike backside straight cracks, Hertzian crack lengths were not influenced by whether or not the impact was blown-out. The Hertzian crack length data had a larger amount of scatter when compared to the backside straight crack length data, particularly at the 1.55 J energy level. The reason for the large variability in Hertzian crack length is unknown but may have to do with the local microstructure and orientation of lamellar grains.

Phases I through IV were performed to satisfy a variety of objectives and the pooled data do not constitute a statistically balanced set of experiments. For example, the thickness of the specimen (and subsequently the leading edge) was only varied in Phases I and II, and therefore, the majority of the data is from the thick samples. Projectile hardness was hard in Phase I, hard and soft in Phase II, and soft in Phases III and IV. Therefore, it is perhaps not surprising that attempts to model the combined data resulted in models that suffered from lack of fit. A small experiment was undertaken to systematically vary energy and X over a wide range. Energy was varied from 0.2 to 2.0 J and X was varied from 0.15 to 1.9 mm. The data were pooled with the existing thick specimen data to model Hertzian and backside straight crack length over a larger range of energy and X and the resulting models are given below. These models are only valid for the thick specimens and variables modeled were E, X, and BO.

$$HCL^{1/2} (mm^{1/2}) = -0.709 \left[\frac{(X - 1.031)}{0.939} \right]^2 + 0.655 \frac{(E - 1.125)}{0.946} - 0.242 \frac{(X - 1.031)}{0.939} - 0.294 \frac{(E - 1.125)}{0.946} * \frac{(X - 1.031)}{0.939} + 1.368; R^2 = 75\% \quad (5)$$

$$\begin{aligned}
BSCL(mm) = & -0.519 \left[\frac{(X - 1.031)}{0.939} \right]^2 - 0.238 \left[\frac{(E - 1.125)}{0.946} \right]^2 + 0.906 \frac{(E - 1.125)}{0.946} \\
& + 0.724 \frac{(X - 1.031)}{0.939} + 1.160[(BO = 1) \text{ or } (noBO = -1)] + 0.515 \frac{(E - 1.125)}{0.946} * \frac{(X - 1.031)}{0.939} \\
& + 3.033; R^2 = 91 \%
\end{aligned} \tag{6}$$

Energy was again the major effect for both the Hertzian crack lengths and the backside straight crack lengths. At low energies, the effect of X was small for Hertzian crack lengths but at high energies, Hertzian crack length reached a maximum at an X distance of approximately 1.0 mm, Figure 14a. Energy had the largest influence on backside straight crack length coming into the model as a main, interactive, and quadratic effect, Figure 14b, but blow-outs and X were also significant factors. At low impact energy (0.2 J), backside crack length increased as X was increased from 0.2 to 1.0 mm and then decreased as X went from 1.0 to 2.0 mm. At an X of 2.0 mm, the low energy impacts did not create backside cracks. Backside cracks continued to increase in length with increasing X at the high energies (2.0 J). The largest X distance studied was 1.9 mm at which point the leading edge still had some curvature and the specimen thickness had not reached its maximum. As stated earlier, the models are only valid over the range of variables studied. At a large enough X distance, the impacts should start to look like thick plate impacts which have a star shaped pattern on the backside instead of a backside crack coming into the width from the leading edge [6].

F. Effect of Impact Damage on Fatigue Strength (Phase III)

Specimens were impacted at energies ranging from 0.2 to 1.55 J to determine the effect of impact energy on fatigue strength. Since thick specimens were shown to have improved impact

resistance in Phase II, only specimens with the thickest leading edge were manufactured for the fatigue studies. After impacting, specimens were tested in high cycle fatigue at 650 °C with a load ratio of 0.05.

Fracture initiation sites were identified based on observations of heat tint on the fracture surfaces and the shape of the fracture surface, Figure 15. A bluish heat tint was observed to be an area of surface-connected cracking that occurred prior to fatigue testing and was clearly distinguishable from the yellowish color on the fracture surface associated with fatigue crack propagation. The fracture initiation site changed with increasing impact energy. Below 0.75 J of impact energy, backside cracks propagated under fatigue loading whereas at higher impact energies, Hertzian cracks propagated. Backside initiated fracture surfaces were generally flat and showed the backside cracks having an elliptical shape. For samples in which fatigue failure initiated from the front side of the specimen, the fracture surface curved around the impact site, following the Hertzian crack, Figure 15d. At the center of the impact, the fatigue crack proceeded across the width of the specimen. Failure initiated from the front (impacted) side of blown-out samples and the fracture surface went straight across the width of the sample from the middle of the blown-out area. The fracture surface morphology changed across the fracture surface of a backside initiated failure, Figure 16. At the leading edge, a rough surface corresponded to the bluish tint on the fracture surface. This was the pre-test crack area that resulted from the ballistic impact. The yellowish-colored fatigue crack growth region had a flat, transgranular fracture morphology and covered less than 5% of the fracture surface. Towards the center of the specimen the fracture surface became rougher containing more intergranular γ cleavage fracture indicating an end to the fatigue crack growth and a transition to tensile

overload. Hertzian initiated failures had a similar transition in fracture morphology but the impact crack initiated on the impact (front) side of the sample. Several non-impacted samples were also fatigue tested and generally failed at internal porosity.

The fatigue strength of Ti-48Al-2Nb-2Cr decreased with increasing impact energy, Figure 17, and while regression predicted the trend, there was still a large amount of scatter resulting in a correlation coefficient of only 70 %. This was because other variables such as X influenced crack severity and subsequent fatigue strength. Fatigue strength was plotted as a function of the crack length that initiated failure, Figure 18. The Hertzian and backside straight crack lengths were measured on the specimen surface after impacting but before fatigue testing. For the as-received samples, the diameter of the internal porosity that initiated failure was plotted in Figure 18. One as-received specimen was defect free and cracks initiated at multiple sites along the gage length and the fatigue strength of this specimen was 343 MPa. While a curve could be visualized to fit all the data in Figure 18, this is somewhat fortuitous as the crack lengths measured represent different geometries with different stress concentration factors. However, the fatigue strength data was better explained by crack length with a correlation coefficient of 86 % compared to only 70% of the variation in fatigue strength data using only impact energy.

Fatigue strength should also be correlated to the cross-sectional area that was cracked prior to fatigue testing. The bluish heat tinted area was measured on the fatigue fracture surfaces and plotted versus fatigue strength in Figure 19. The cross-sectional area of the pores were used for the “defect area” of as-received samples. Pre-crack area was a poor predictor of maximum

fatigue strength, accounting for only 56% of the variation in the data. One sample was impacted at a low energy, 0.36 J, but X was unusually large (1.45 mm) for two of the three impacts on the sample, including the impact that initiated failure. The backside straight cracks were narrow but long, one of which extended a distance of 1.45 mm. The resulting fatigue strength was unusually low for a sample impacted with this low energy, Figure 17, and could not be predicted by the small crack area. Backside straight crack length or Hertzian crack length (for front initiated failure) was better correlated to the residual fatigue life than pre-test crack area.

Every sample was impacted at three different locations but only one impact site initiated failure. The impact sites that did not lead to fatigue failure were examined after fatigue testing. In all the examined specimens, the cracks from these impacts failed to propagate during the fatigue test, Figure 20, which suggests that propagation only occurred on the final load increment and only one impact was needed for studying residual fatigue properties. For backside initiated failures, the impact that had the largest backside straight crack was the impact that initiated failure in 13 of the 17 samples (76%). For another two samples, failure occurred at the impact that had the largest X but not the largest backside crack. In one of these samples, failure initiated at a single, continuous backside crack instead of a longer but non-continuous set of backside cracks, Figure 21. While the correlation with Hertzian crack length and fatigue initiation site was not as strong, half of the Hertzian initiated samples did fail at the impact with the largest (or very close to largest) Hertzian crack length.

G. Effect of Mean Stress on Fatigue Strength (Phase IV)

The effect of tensile mean stress on the fatigue strength of specimens impacted at two energies, 0.71 and 1.52 J, was evaluated. Four impacted samples were tested at each of 3 load-ratios, 0.05, 0.2, and 0.5, such that a total of 12 specimens were tested for each energy level. The results show a classical mean stress dependence of the fatigue strength as shown using a Goodman Diagram, Figure 22. Additional data with impact energies ranging between 0.2 and 1.5 J are also included in Figure 22 along with a line representing cylindrically-shaped, smooth bar specimens tested by GE. The datum for the defect-free, as-received sample from this study lies near the smooth bar line. This was despite the somewhat sharp edges and rough, as-cast and chem-milled surface of the samples used in the current study. The data in Fig. 22 fall into two groups independent of load ratio. These two groups represent the two different impact energy levels. It appears as if both mean stress curves and the curve from the smooth bar data extrapolate to points between the 0.2% YS and the UTS of the material.

Fatigue strength using crack length could not be effectively modeled due to the two different crack types that initiated fatigue failure. However, the effect of impact energy, load-ratio, X , and blow-outs on the fatigue life was analyzed using multiple regression. Fatigue strengths for both failure initiation sites are included and interactive and quadratic terms were allowed. The resulting model is given below:

$$\text{Fatigue Strength, MPa} = -55.3 \frac{(E - 0.90)}{0.68} - 36.1 \frac{(X - 1.17)}{0.71} + 33.3 \frac{(R - 0.25)}{0.25} + 199.9; \quad R^2 = 80\% \quad (7)$$

Impact energy was again the most important variable but X and load ratio were also significant factors in predicting fatigue strength.

V. Discussion

Of the impact variables studied, impact energy, specimen thickness, projectile hardness, and impact temperature, impact energy had the largest influence on the response of γ - TiAl to impact damage. Thickness was also an important variable over the range of energy used in Phase II, 0.05 to 0.33 J, with the thick specimens exhibiting improved impact resistance. However, the significance of thickness on crack length was diminished at the higher ranges of energy. The effect of impact damage on the fatigue strength of thinner samples should be investigated, as thick leading edges are contrary to establishing good aerodynamics.

X, the distance from the center of the impact to the leading edge, was held as constant as possible for all the phases but varied due to the nature of the testing. The variation in X was small enough in Phase II that X was only a minor main effect for the Hertzian crack length model and was not included as a main effect for the backside models. However, the variation in X was more significant in later phases and the effect of X on both crack lengths and fatigue strength was found to be significant. The backside straight crack length increased with X, within the range of X tested, whereas the Hertzian crack length reached a maximum at an X distance of approximately 1.0 mm for the thick specimens.

The effect of temperature on the impact resistance of TiAl was studied in the side experiment using the thick specimens and impacting at 0.19 J of energy. Energy was held as constant as possible for this experiment, yet energy and temperature had similar coefficients for both Hertzian and backside straight crack lengths. In other words, a small range of impact energy was equivalent to a large range in impact temperature. Cracking of TiAl due to ballistic impacts has been shown to be controlled more by levels of strain than stress [6]. At high strain rates, the work hardening rate of γ -Ti-47Al-2Nb-2Cr is constant from 25 to 1100 °C [7]. The small effect of temperature on the impact resistance of TiAl is probably due to the high strain rate occurring during a ballistic impact test and the constant work hardening at the high strain rate. A large amount of scatter was observed in the crack length data at 23 °C. The large scatter could partially be attributed to variations in X but may also be attributed to the higher flow stress and more brittle nature of the material at 23 °C. The impact cracks traverse many grains and a large volume of material such that the effect of individual grain microstructure was not obvious.

Separate models describing crack lengths were developed for Phase II and for Phases I-IV. The Phase II models covered a smaller energy range but incorporated all three thicknesses of samples. Phase II was a designed set of experiments and therefore the models had slightly higher correlation coefficients than the models developed for Phases I-IV. However, there was considerable similarity between the two sets of models. Energy was the most important variable for all models. The effect of X on crack length was more significant when all of the data was combined due to the larger range of X. As previously mentioned, the presence of “blow-outs” was important to backside straight crack length for both Phase II and Phases I-IV due to the

method of measurement. The larger range of E and X available with the combined data led to a X^2 term in the Hertzian crack length model and E^2 and X^2 terms included in the BSCL model for Phases I – IV. A fairly high percentage, 75 to 91 percent, of the data could be explained by the various models obtained.

The step test approach to fatigue testing significantly reduced the number of required samples since runouts were not allowed. It is believed that crack propagation occurred on the last step interval, based on the following two reasons. The non-failure impacts were examined and the surface cracks did not propagate. Additionally, of the 37 samples fatigue tested, 34 failed early in the final step, at less than 50,000 cycles. Thus, the penultimate stress level is a reasonable approximation of the fatigue threshold. Any stress below this value will not cause the cracks to propagate and any stress above this value causes rapid failure due to the steepness of the crack propagation curve. Step testing has been compared to conventional fatigue testing on stainless steels [4]. With block lengths of 50,000 or more cycles and stress increments of 1%, the fatigue strength of step tested material fell within the scatterbands of the conventional tests. Step fatigue testing of TiAl has been modeled using stress increments of 10 MPa and it was shown that increasing the block size (i.e., the number of cycles) increased the accuracy of the model compared to experimental data [8]. The step tests done in this study utilized step sizes of 7 to 14 MPa and block lengths of 10^6 to 10^7 cycles both of which should be sufficient to achieve accurate results.

The fatigue failure stress of Ti-48Al-2Nb-2Cr after impact damage has been predicted using a threshold –based approach [6,9]. Impact damage was simulated by indenting the sample

edge with a sharp steel wedge resulting in a through thickness wedge-shaped indent. When the effective crack length exceeded a transitional value (100 μm for Ti-48Al-2Nb-2Cr), the fatigue failure stress could be predicted using the threshold based approach. For similar fatigue strengths, the cracks measured on the same alloy in this study were substantially longer. The cracks induced by ballistic impacting are not through thickness cracks and have a complex geometry. For an accurate prediction of the fatigue failure stress, a stress intensity approach should be applied to each crack shape. However, crack geometries can only be measured on the fracture surfaces post fatigue testing. Prior to fatigue testing, the best estimation of fatigue strength for this type of impact and specimen is the plot of backside crack length or Hertzian crack length as a function of maximum fatigue strength, Figure 18. The other crack dimensions are unknown and could significantly influence the stress intensity factor and hence which crack actually propagates. Given an exact crack geometry, stress intensity factors can be utilized to accurately predict fatigue strength as will be shown in a future paper.

The impacted TiAl displayed a classical mean stress dependence of the fatigue strength, Fig. 22. Despite considerable variability in the crack lengths, particularly for Hertzian crack lengths, the fatigue strength was fairly repeatable for a particular impact condition and load-ratio. Samples were impacted at three locations to normalize the effects of variability in microstructure and to minimize the scatter in fatigue data. Given the good repeatability in fatigue strength, one impact per specimen would have been sufficient, however, the multiple impacts were useful in obtaining additional impact crack length data. The impact that initiated failure could also be

directly compared to the other two, non-failure impacts to see if the other cracks propagated during fatigue.

Backside straight crack lengths are a logical choice for predicting fatigue strength as the cracks run perpendicular to the loading axis. However, the Hertzian crack length is not as natural of a choice as the Hertzian cracks run at an angle to the stress axis. Predicting which of the three impacts would initiate failure was not as accurate with Hertzian crack lengths as with backside straight cracks. However, Hertzian crack lengths explained approximately 70% of the fatigue strength data initiated by Hertzian cracks, the same as for backside straight crack lengths explained for backside initiated failures. Another possible predictive measurement for front side initiated failures would be the distance from the leading edge to the start of the Hertzian crack next to the impact dent. However, this measurement did not vary much as a function of impact energy. Pre-crack area on the fracture surface, besides not being a predictive measurement, only described 56% of the data.

This program was initiated to determine if Ti-48Al-2Nb-2Cr low pressure turbine blades could survive an impact event in the 6th and last stage of a GE90 engine. The fatigue design requirement for this particular application is to survive 10^7 cycles at a maximum stress of 140 MPa. Short of a catastrophic event, impact damage is not expected at this location in the engine. However, honeycomb debris has been found in test engines and could conceivably cause impact damage on these blades. This is a concern due to the low ductility and rapid crack propagation rates of γ -TiAl. The energy associated with these honeycomb pieces in an engine would be on

the order of 0.05 to 0.3 J. On the thick specimens, backside cracking was observed for impacts with energies of 0.17 J or higher, and this could conceivably lead to fatigue failure of the component. However, this study showed that specimens easily met the fatigue design requirements for impacts with 0.05 to 0.3 J of energy. Cracks formed from these energy levels would not propagate under normal service loads and therefore LPT blades similar in thickness would not fail. It would take a fairly large impact event, 1.5 J or higher of energy, to fail Ti-48Al-2Nb-2Cr LPT blades in this application.

VI. Summary and Conclusions

The experimental impact conditions chosen produced a spectrum of damage from minor denting to blowing-out a piece of the specimen's edge. Multiple linear regression was used to model the cracking and fatigue response as a function of impact variables. Of the impact variables studied, impact energy had the largest influence on the response of γ - TiAl to ballistic impacting. The fatigue initiation sites depended on impact energy, with the lower energy (<0.74 J) impacted samples failing from backside cracks and higher energy (>0.74 J) impacted samples failing from front or Hertzian cracks. Fatigue testing using the step method allowed the assessment of impact damage on fatigue strength while significantly reducing the number of required samples by eliminating runouts. The best estimation of the fatigue strength for this type of impact and specimen was a plot of crack length as a function of maximum fatigue strength. The impacted γ -TiAl samples showed a classical mean stress dependence on the fatigue strength. Given the fatigue design stresses, a Ti-48Al-2Nb-2Cr LPT blade would survive an impact of normal service oriented conditions. It would take a large impact event of 1.5 J or higher of

energy, as might result from a catastrophic event, to cause impact damage large enough to fail a Ti-48Al-2Nb-2Cr low pressure turbine blade by service related fatigue.

Bibliography

1. C.M. Austin; T.J. Kelly; K.G. McAllister, and J.C. Chesnutt: *Structural Intermetallics 1997*, TMS Symp. Proc., M.V. Nathal, R. Darolia, C.T. Liu, P.L. Martin, D.B. Miracle, R. Wagner, and M. Yamaguchi, eds., TMS, Warrendale, PA, 1997, p. 413-25.
2. J.M. Larsen; B.D. Worth; S.J. Balsone, and J.W. Jones: *Gamma Titanium Aluminides*, Y.W. Kim, R. Wagner, and M. Yamaguchi, eds., TMS, Warrendale, PA, 1995, pp. 821-834.
3. J.A. Collins: *Failure of Materials in Mechanical Design*, John Wiley & Sons, New York, NY, 1993, pp. 379-81.
4. J. Denk, and S. Amhof: *Fatigue '96: Proc. of 6th Int. Fatigue Congr.*, Vol. III, G. Lutjering and H. Nowack, eds., Pergamon Press, 1996, pp. 1967-1972.
5. H. Hertz: *J. Reine Angew. Math.*, **92** (1881), pg. 156; translated and reprinted in English in "Hertz's Miscellaneous Papers," Macmillan, New York, 1896, Ch. 5.
6. P.S. Steif; J.W. Jones; T. Harding; M.P. Rubal; V.Z. Gandelman; N. Biery, and T.M. Pollock: *Structural Intermetallics 1997*, M.V. Nathal, R. Darolia, C.T. Liu, P.L. Martin, D.B. Miracle, R. Wagner, and M. Yamaguchi, eds., TMS, Warrendale, PA, 1997, pp. 435-42.
7. S.A. Maloy and G.T. Gray III: *Acta Metall.*, Vol. 44, No. 5, 1996, pp. 1741-56.
8. T. Harding and J.W. Jones: Year 2 PRET Review, Carnegie Mellon University, Pittsburgh, PA, May 1997.
9. T.S. Harding; J.W. Jones; P.S. Steif, and T.M. Pollock: *Scripta Metall.*, Vol. 40, No. 4, 1999, pp. 445-9.

Tables

Table I. Alloy Chemistry

Table II. Tensile Properties of Impact Specimens from both Castings

Table III. Summary of Crack Length Models for Phase II

Figure Captions

Figure 1. a) Design of experiments (DOE) for Phase I (● - 3.2 mm projectiles) and Phase II (○ - 1.6 mm projectiles). b) temperature side experiment utilized thick specimens and an energy of 0.19 J.

Figure 2. Cast-to-shape impact specimen design.

Figure 3. Ballistic impact rig setup.

Figure 4. Front (a) and backside (b) crack measurements. The impact location, “X”, is also shown in (a).

Figure 5. Typical microstructure of (a) Casting 1 (Phases I and II) and (b) Casting 2 (Phases III and IV).

Figure 6. Front and corresponding backside damage from low energy ($E=0.05$ J) impacts. (a) front of thin sample, (b) front of thick sample, and (c) backside of thin sample. Backside cracks were not detected on surface of thick sample impacted at low energy. All impacts used 1.6 mm projectiles.

Figure 7. Front and corresponding backside damage after impacting with 0.33 J of energy. Fatigue stress axis (a) is parallel to specimen edge and perpendicular to backside cracks. (a) front of thin sample, (b) front of thick sample, (c) backside of thin sample and (d) backside of thick sample. All impacts used 1.6 mm projectiles. The thin sample (a and c) was nearly blown-out and the backside straight crack length measurement for a near blow-out or a blow-out is demonstrated.

Figure 8. Backside crack length plotted as a function of impact energy. Data for soft and hard projectiles were pooled. Thick specimens exhibited improved crack resistance for the energy range used in Phase II.

Figure 9. 3-D plots of Phase II Hertzian crack length model for (a) thin, (b) medium, and (c) thick samples.

Figure 10. 3-D plots for Phase II backside straight crack length for (a) thin, (b) medium, and (c) thick samples using projectiles with a hardness of 40 HRC and no blow-outs.

Figure 11. Results of temperature side experiment: (a) Hertzian crack length and (b) backside straight crack length. Variations in energy and X contributed to scatter in data.

Figure 12. 3-D plots of temperature side experiment models for Hertzian crack length (a,b) and backside straight crack length (c,d).

Figure 13. Effect of impact energy on (a) Hertzian crack length and (b) backside straight crack length for all four phases. All samples impacted at 260 °C. The majority of data within circles are for blown-out impacts.

Figure 14. 3-D plots depicting (a) Hertzian crack length and (b) backside crack length over a large range of energy and X. Models only valid for thick specimens impacted at 260 °C with no blow-outs.

Figure 15. Fatigue fracture surfaces of (a) backside initiated, (b) Hertzian initiated, and (c) blown-out samples. (d) Hertzian initiated fracture surfaces follow circumferential cracks around the impact site and then traverse the specimen at a cross-section near the center of the impact.

Figure 16. Fracture morphology change across the surface of a backside initiated fatigue sample.

Figure 17. Fatigue initiation site changed from backside to Hertzian crack initiation with increasing impact energy. Fatigue crack initiation of as-received samples occurred primarily at internal porosity. All data shown in this plot were generated at $R = 0.05$.

Figure 18. Fatigue strength was correlated to impact crack length or internal defect diameter for as-received samples. All data shown in this plot were generated at $R = 0.05$.

Figure 19. Fatigue strength was not strongly correlated to impact crack area or defect area.

Figure 20. Surface cracks of a non-failure impact site did not propagate during fatigue testing.

(a) Front and (c) backside of impact before fatigue testing, (b) front and (d) backside of impact after fatigue testing. Sample was impacted with 3.2 mm projectile at 1.05 J of energy. Fatigue failure initiated from a different impact site on the same specimen.

Figure 21. Wider, straighter backside crack of (a) initiated the fatigue failure of this sample instead of the longer but branched backside crack shown in (b).

Figure 22. Goodman diagram for two impact energies, $E = 0.71$ J and $E = 1.52$ J. Fatigue tests were run at 100 Hz and 650 °C.

Table I – Alloy Chemistry

	Composition, at. %						
	Ti	Al	Cr	Nb	C	N	O
Microstructural DOE (Phases I and II)	47.9	48.0	1.94	1.96	0.013	0.014	0.167
Fatigue Study (Phases III and IV)	48.4	47.5	1.87	1.97	0.019	0.018	0.212

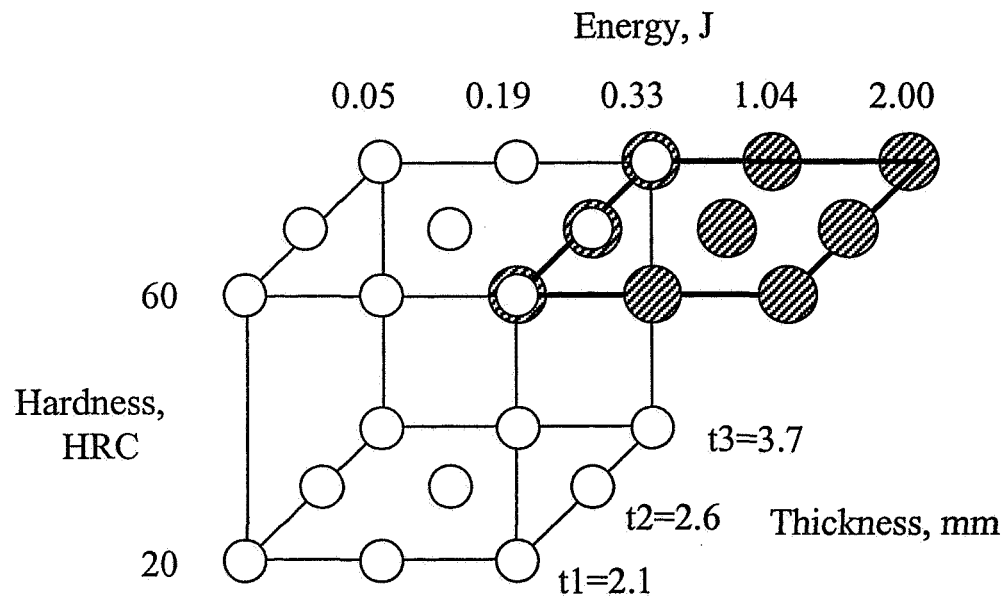
Table II. Tensile Properties of Impact Specimens from both Castings

Casting	Temp., °C	No. of tests	$\sigma_y \pm 95\%$ C.I., MPa	UTS $\pm 95\%$ C.I., MPa	$\epsilon_p \pm 95\%$ C.I., %	E $\pm 95\%$ C.I., GPa
1	23	5	304 ± 19	401 ± 27	1.86 ± 0.20	177 ± 29
1	650	2	269 ± 109	447 ± 201	4.7 ± 6.0	143 ± 140
2	23	8	326 ± 13	422 ± 14	1.70 ± 0.20	168 ± 15
2	650	4	284 ± 29	474 ± 102	5.1 ± 3.3	141 ± 20

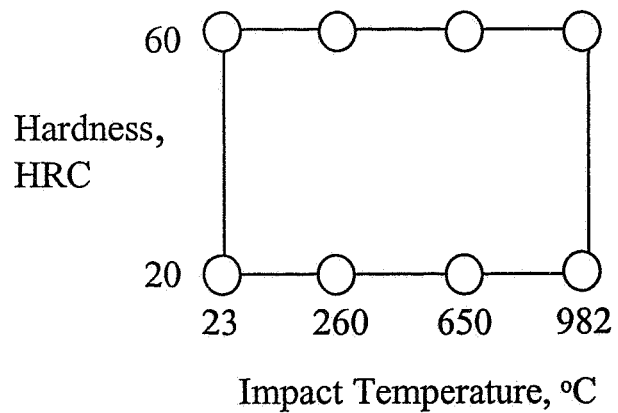
Table III. Summary of Crack Length Models for Phase II

Phase II	Main Effects					Interactive Effects						Quadratic Effects			R ²
Crack Type	E	t	H	X	BO	Et	EH	EX	tH	tX	HX	E ²	t ²	X ²	
Front Major	+	-		-								+	-		86
Front Total	+	-	+		+		+								87
Hertzian SQRT	+	-		-				-		+					89
Back Straight	+	-	-		+			-	+	+				+	91
Back Total	+	-				-				+			+		85

* +/- indicates increase or decrease in crack length from factor. Most significant factors are bolded. Empty boxes indicates factor was not significant and not included in the model.



a.) DOE for Phases I and II. All impacts at 260 °C



b.) DOE for Temperature Side Experiment

Figure 1. a.) Design of experiments (DOE) for Phase I (● - 3.2 mm projectiles) and Phase II (○ - 1.6 mm projectiles). b.) temperature side experiment utilized thick specimens and an energy of 0.19 J.

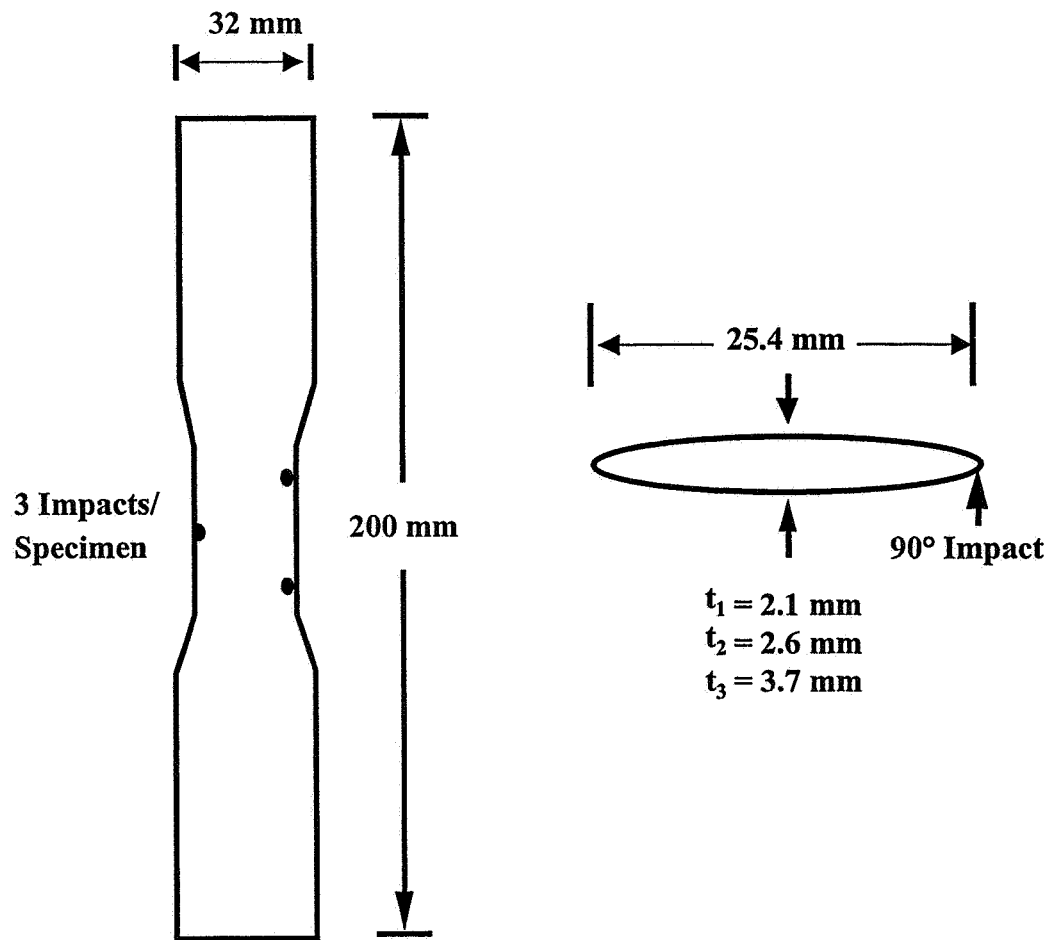


Figure 2. Cast-to-shape impact specimen design

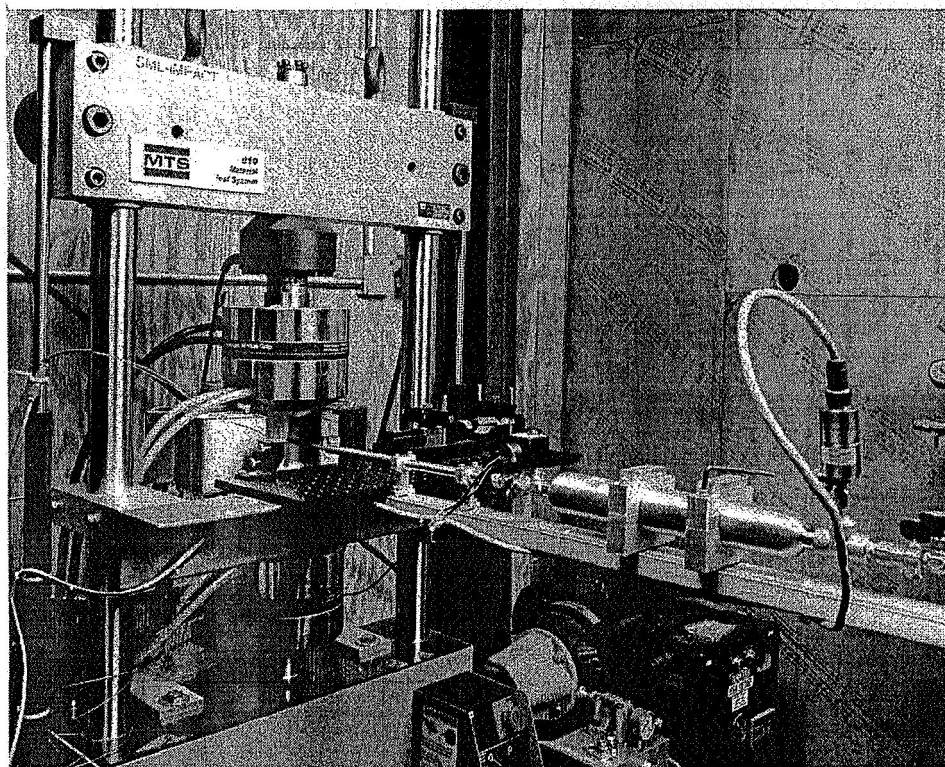
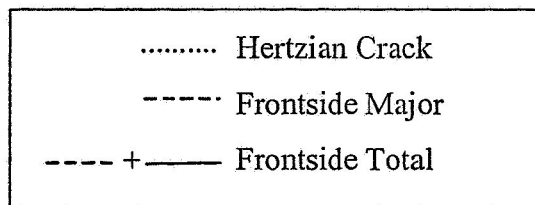
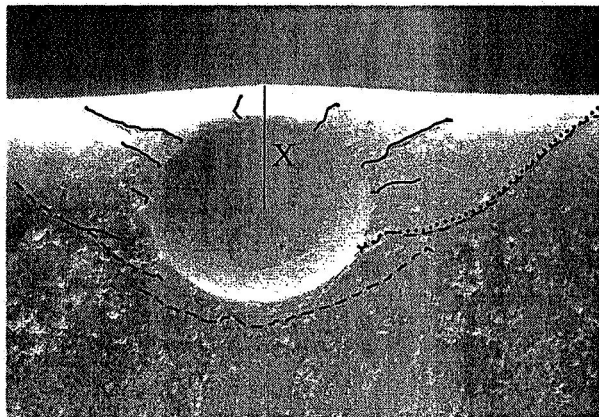
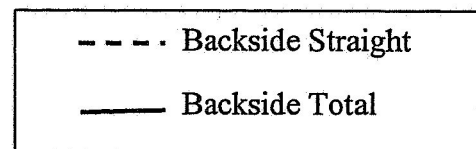
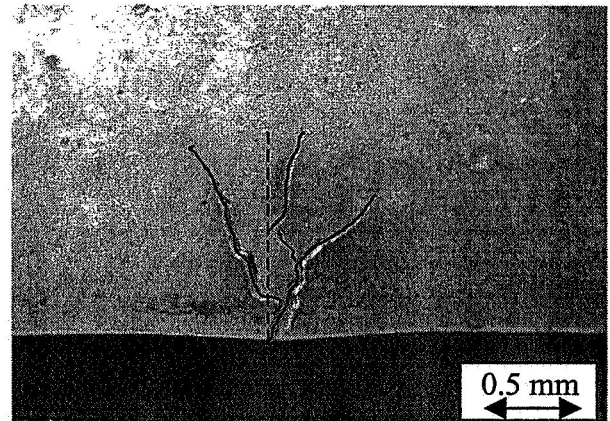


Figure 3. Ballistic impact rig setup.



(a)

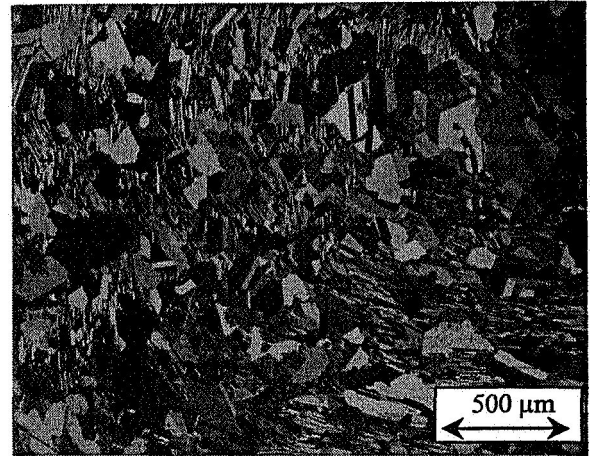


(b)

Figure 4. Front (a) and backside (b) crack measurements. The impact location, "X", is also shown in (a).

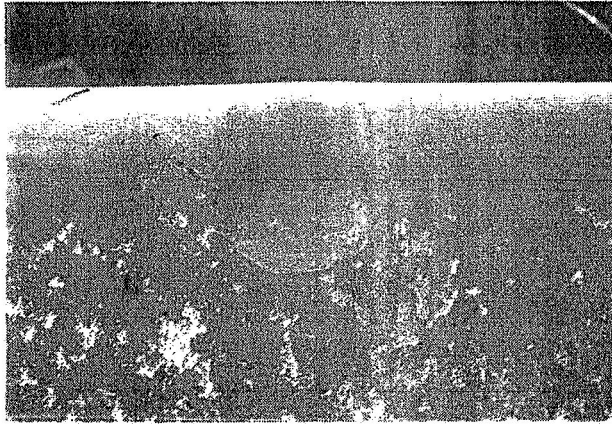


(a)

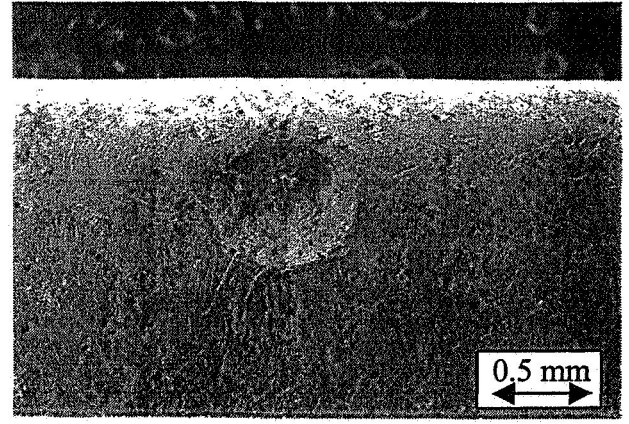


(b)

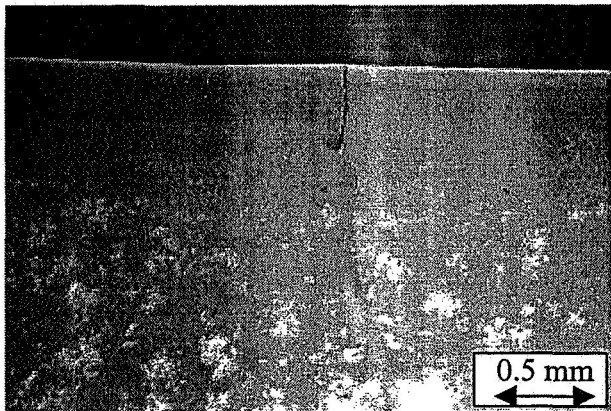
Figure 5. Typical Microstructure of (a) Casting 1 (Phases I and II) and (b) Casting 2 (Phases III and IV).



(a)

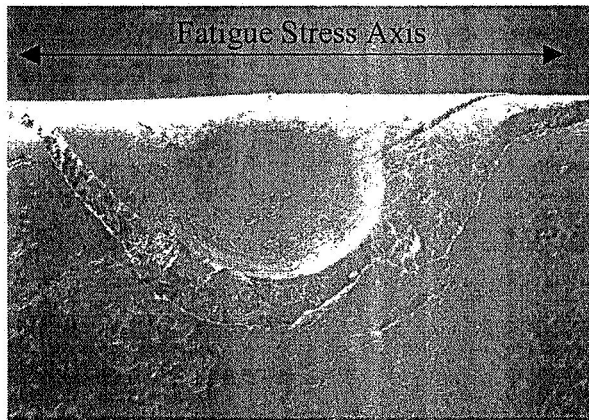


(b)

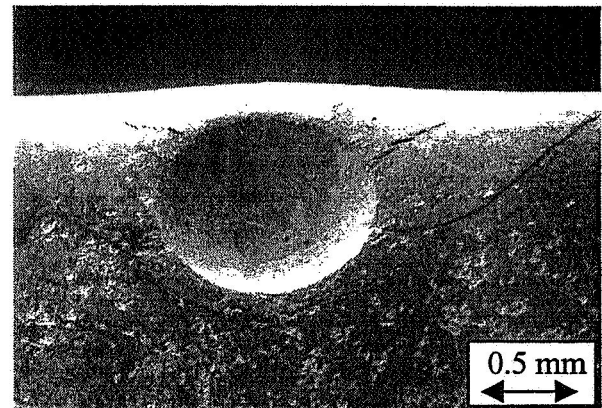


(c)

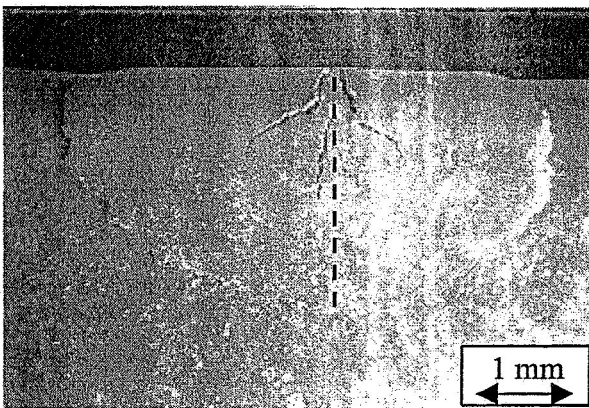
Figure 6. Front and corresponding backside damage from low energy ($E = 0.05$ J) impacts. (a) front of thin sample, (b) front of thick sample, and (c) backside of thin sample. Backside cracks were not detected on surface of thick sample impacted at low energy. All impacts used 1.6 mm projectiles.



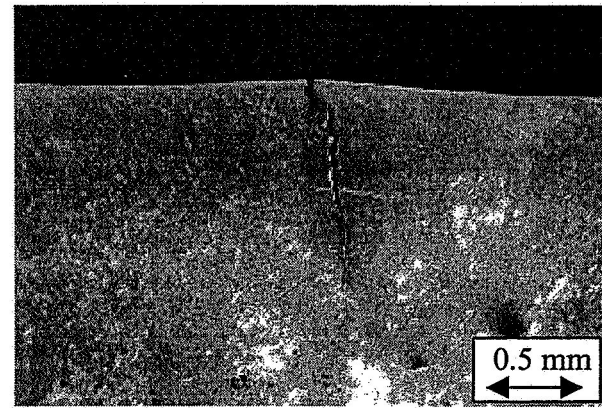
(a)



(b)



(c)



(d)

Figure 7. Front and corresponding backside damage after impacting with 0.33 J of energy. Fatigue stress axis (a) is parallel to specimen edge and perpendicular to backside cracks. (a) front of thin sample, (b) front of thick sample, (c) backside of thin sample and (d) backside of thick sample. All impacts used 1.6 mm projectiles. The thin sample (a and c) was nearly blown-out and the backside straight crack length measurement for a near blow-out or a blow-out is demonstrated.

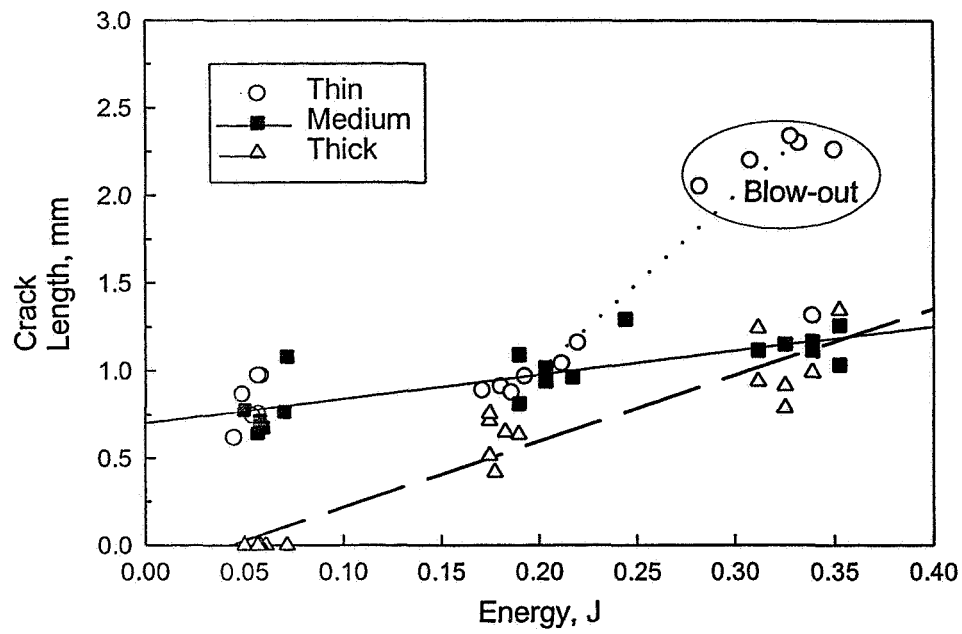
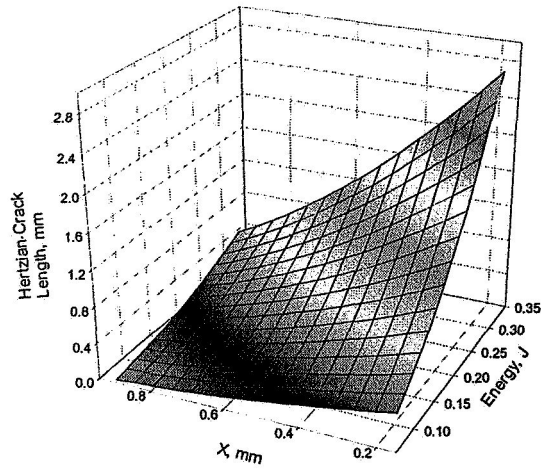
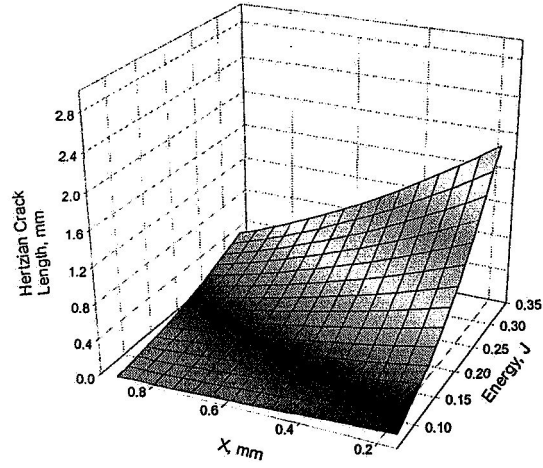


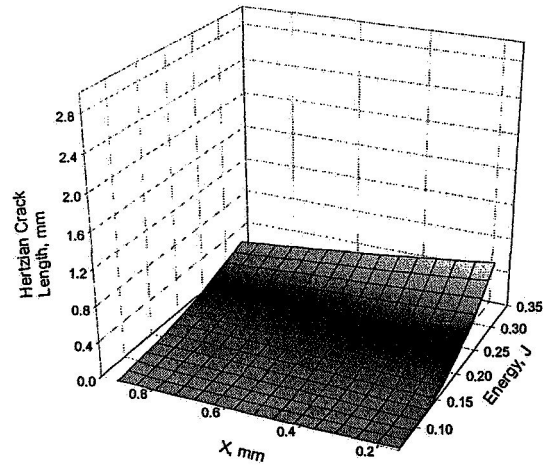
Figure 8. Backside crack length plotted as a function of impact energy. Data for soft and hard projectiles were pooled. Thick specimens exhibited improved crack resistance for the energy range used in Phase II.



(a)

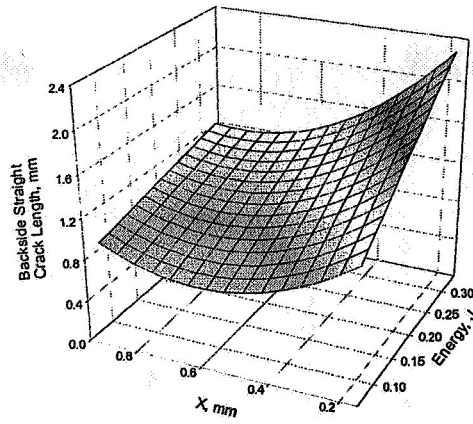


(b)

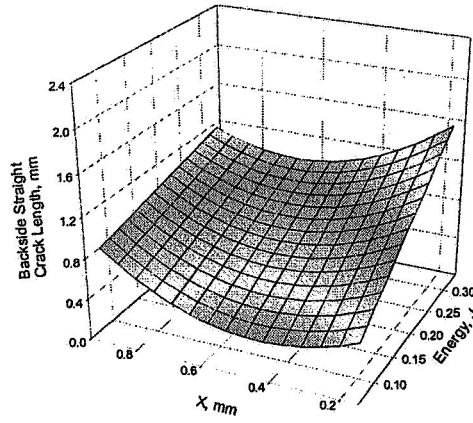


(c)

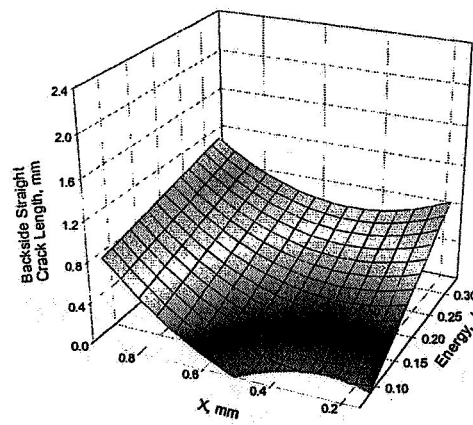
Figure 9. 3-D plots of Phase II Hertzian Crack Length model for (a) thin, (b) medium, and (c) thick samples.



(a)

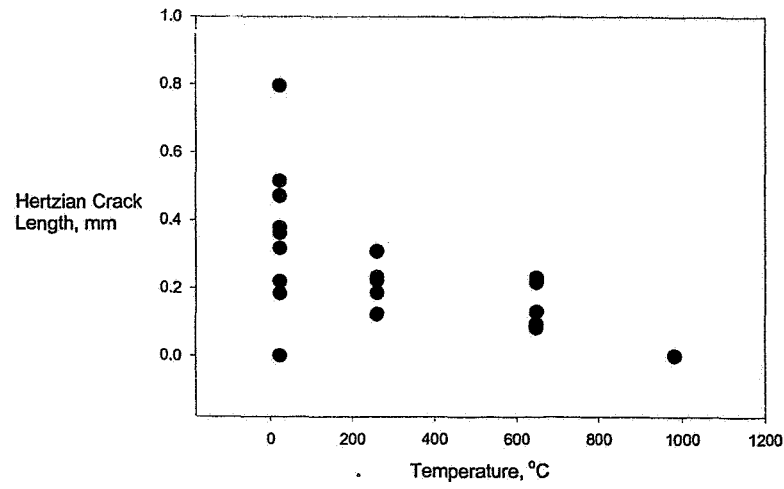


(b)

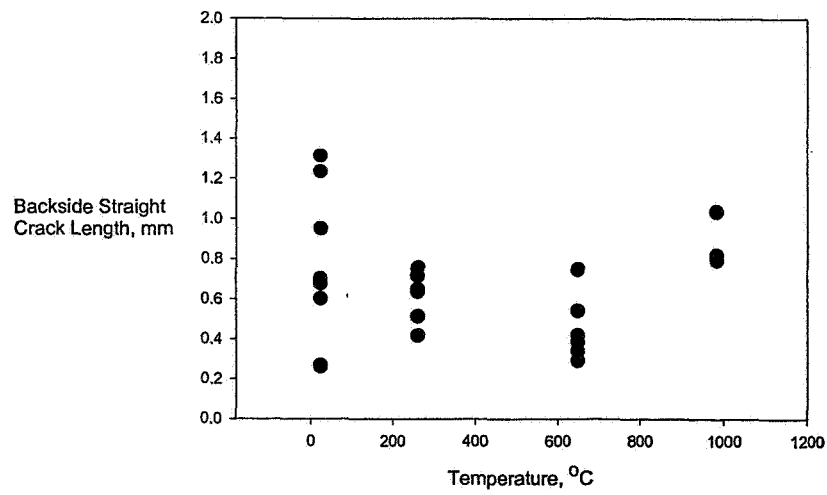


(c)

Figure 10. 3-D plots of Phase II backside straight crack length model for (a) thin, (b) medium, and (c) thick samples using projectiles with a hardness of 40 HRC and no blow-outs.

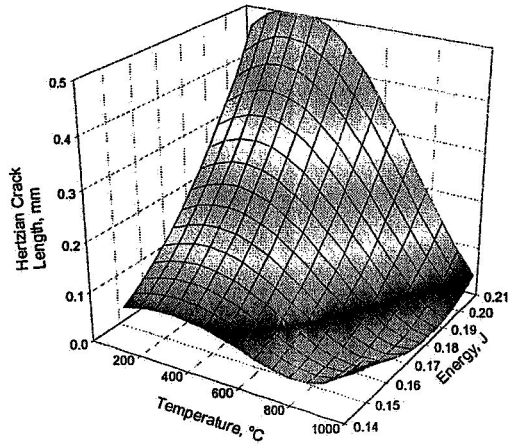


(a)

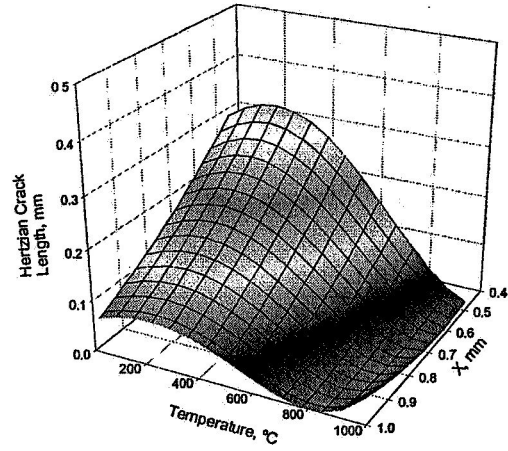


(b)

Figure 11. Results of temperature side experiment: (a) Hertzian crack length and (b) backside straight crack length. Variations in energy and X contributed to scatter in data.

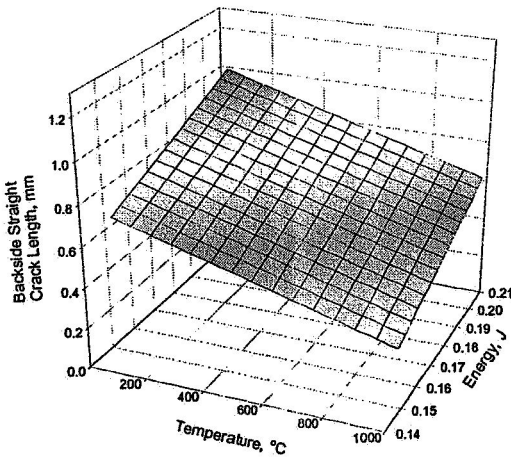


(a) $X = 0.73$ mm

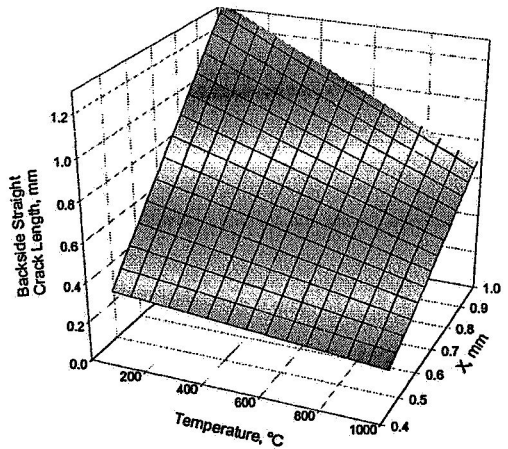


(b) $E = 0.18$ J

Note x axis is reversed for clarity.

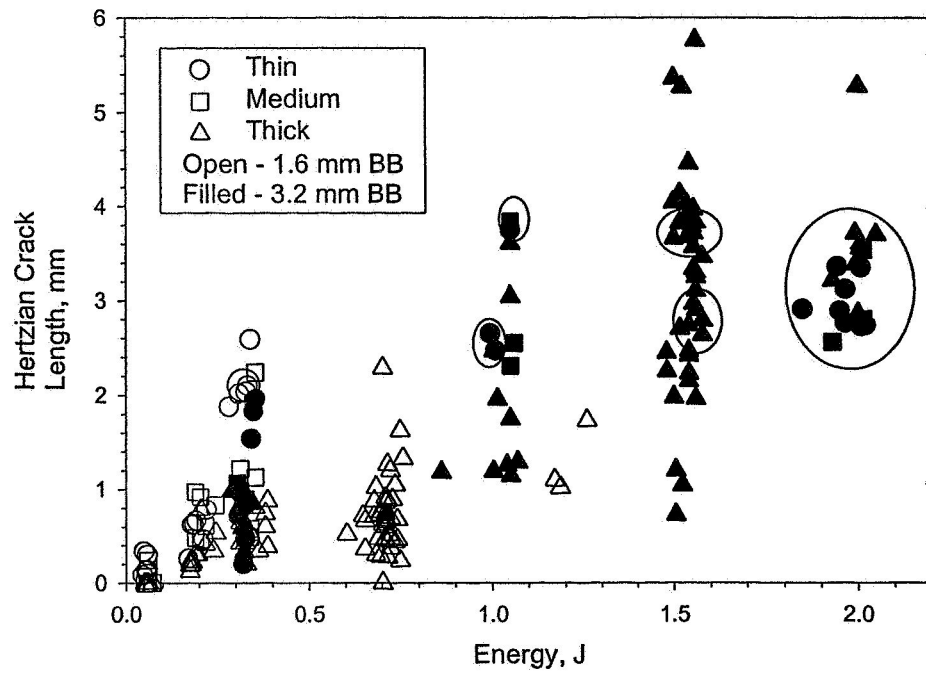


(c) $X = 0.73$

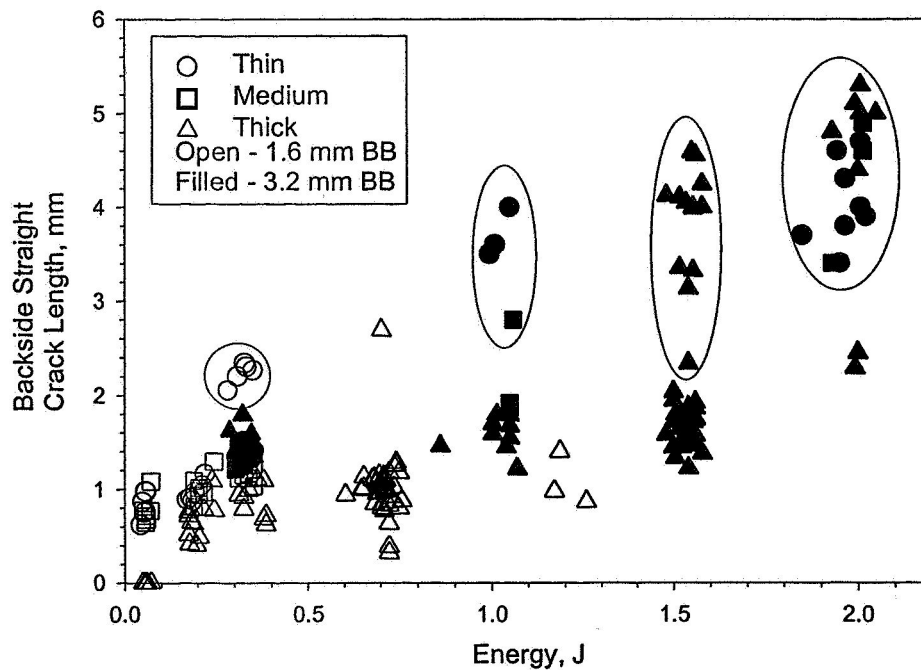


(d) $E = 0.18$ J

Figure 12. 3-D plots of temperature side experiment models for Hertzian crack length (a, b) and backside straight crack length (c,d).

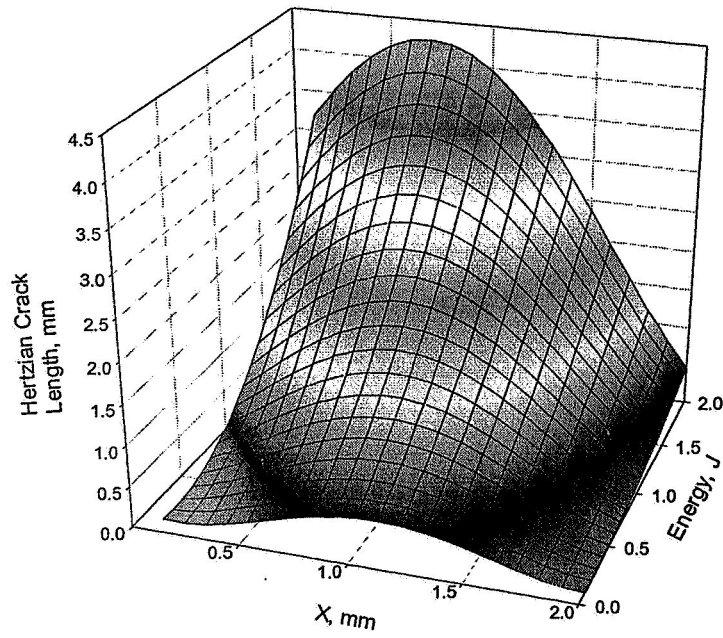


(a)

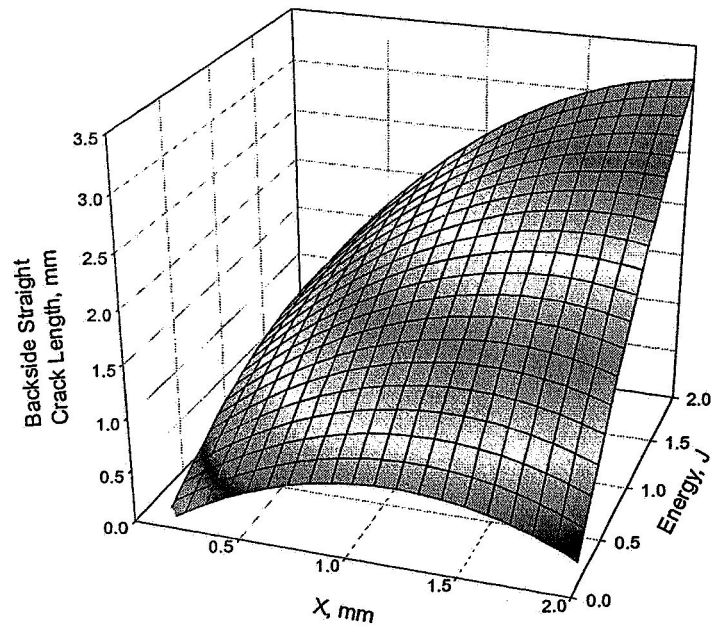


(b)

Figure 13. Effect of impact energy on (a) Hertzian crack length and (b) backside straight crack length for all four phases. All samples impacted at 260 °C. The majority of data within circles are for blown-out impacts.

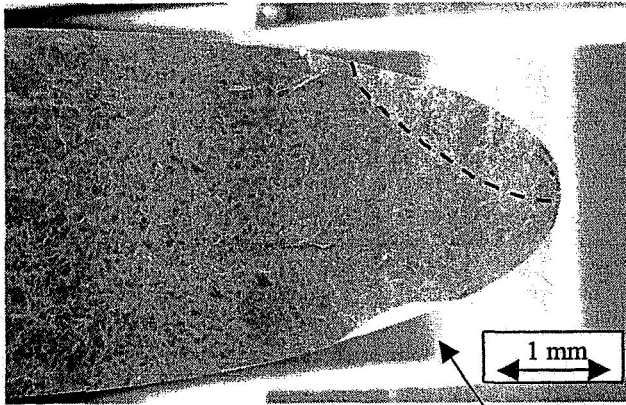


(a)

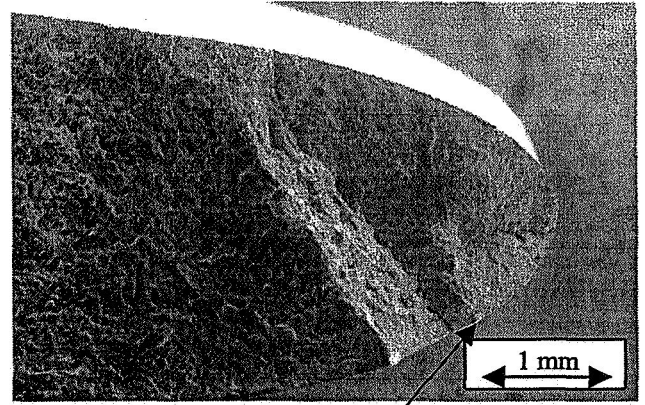


(b)

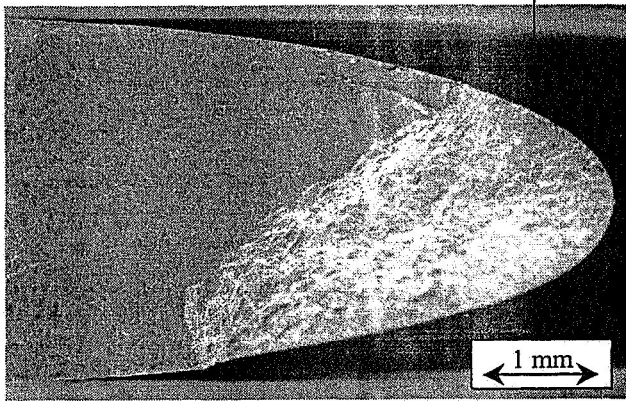
Figure 14. 3-D plots depicting (a) Hertzian crack length and (b) backside crack length over a large range of energy and X. Models only valid for thick specimens impacted at 260 °C with no blow-outs.



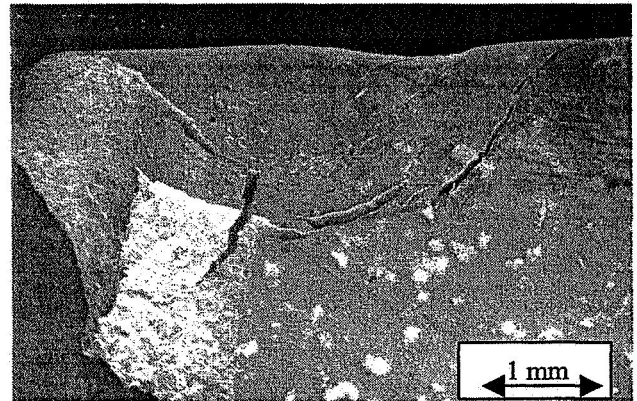
(a) $E = 0.33 \text{ J}$ Impact Site



Impact Site
(b) $E = 0.74 \text{ J}$



(c) $E = 1.52 \text{ J}$



(d) $E = 1.04 \text{ J}$

Figure 15. Fatigue fracture surfaces of (a) backside initiated, (b) Hertzian initiated, and (c) blown-out samples. (d) Hertzian initiated fracture surfaces follow circumferential cracks around the impact site and then traverse the specimen at a cross-section near the center of the impact.

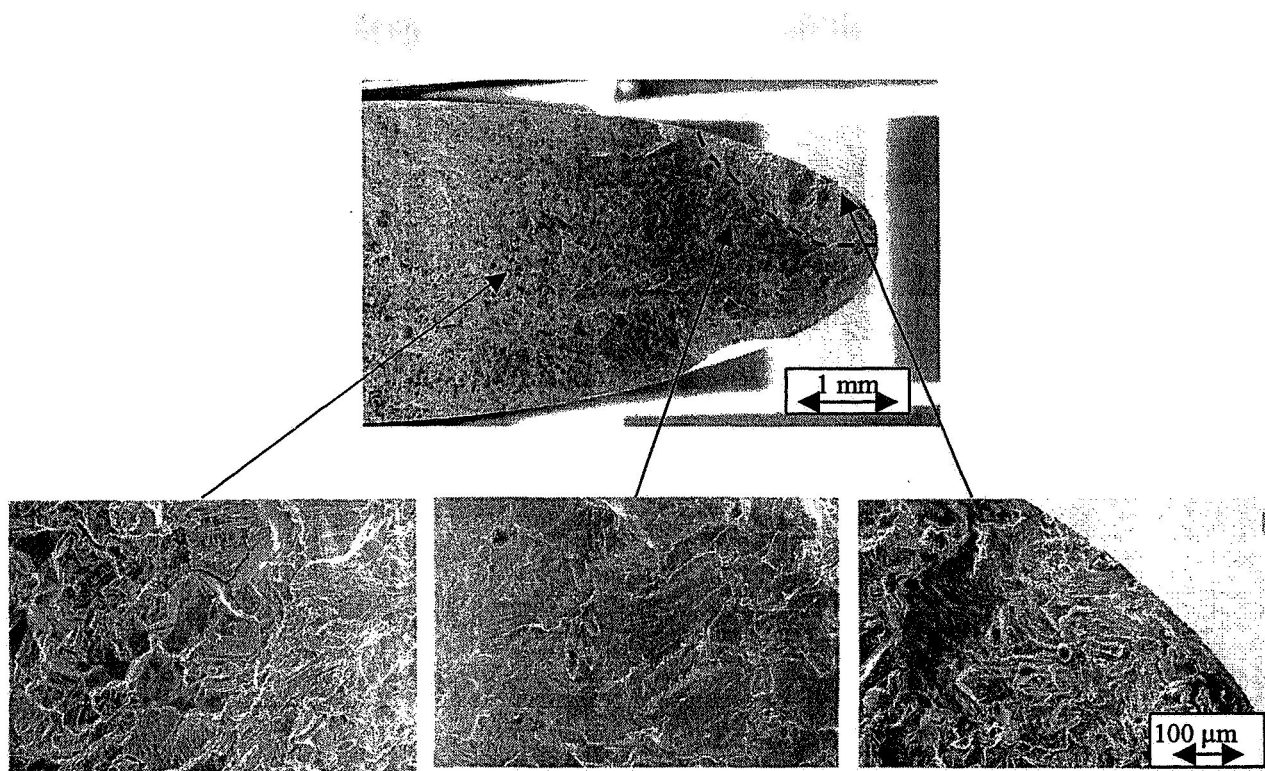


Figure 16. Fracture morphology change across the surface of a backside initiated fatigue sample.

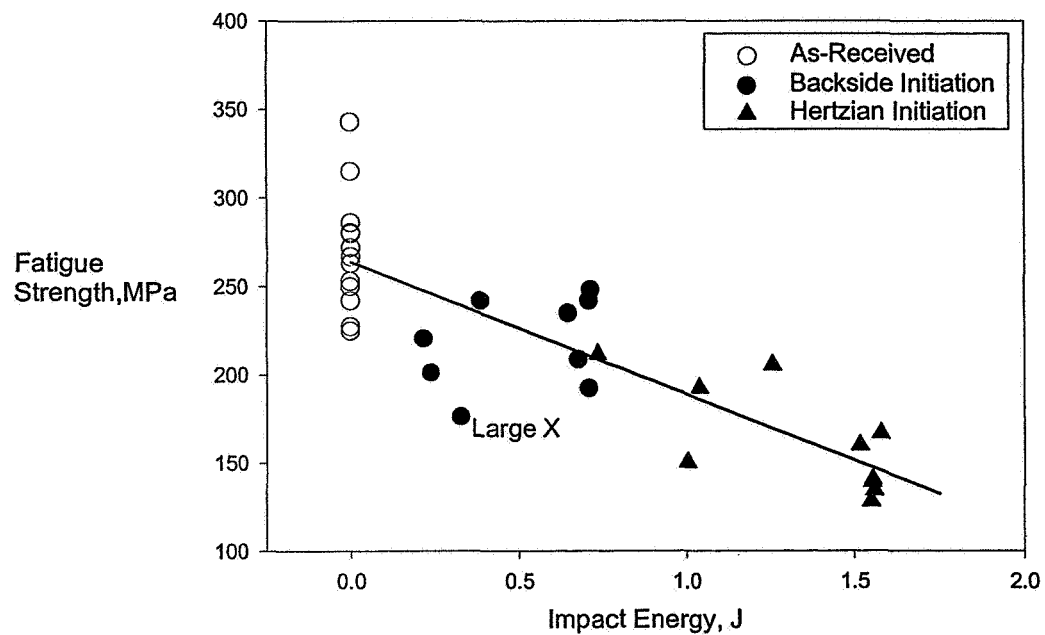


Figure 17. Fatigue initiation site changed from backside to Hertzian crack initiation with increasing impact energy. Fatigue crack initiation of as-received samples occurred primarily at internal porosity. All data shown in this plot were generated at $R=0.05$.

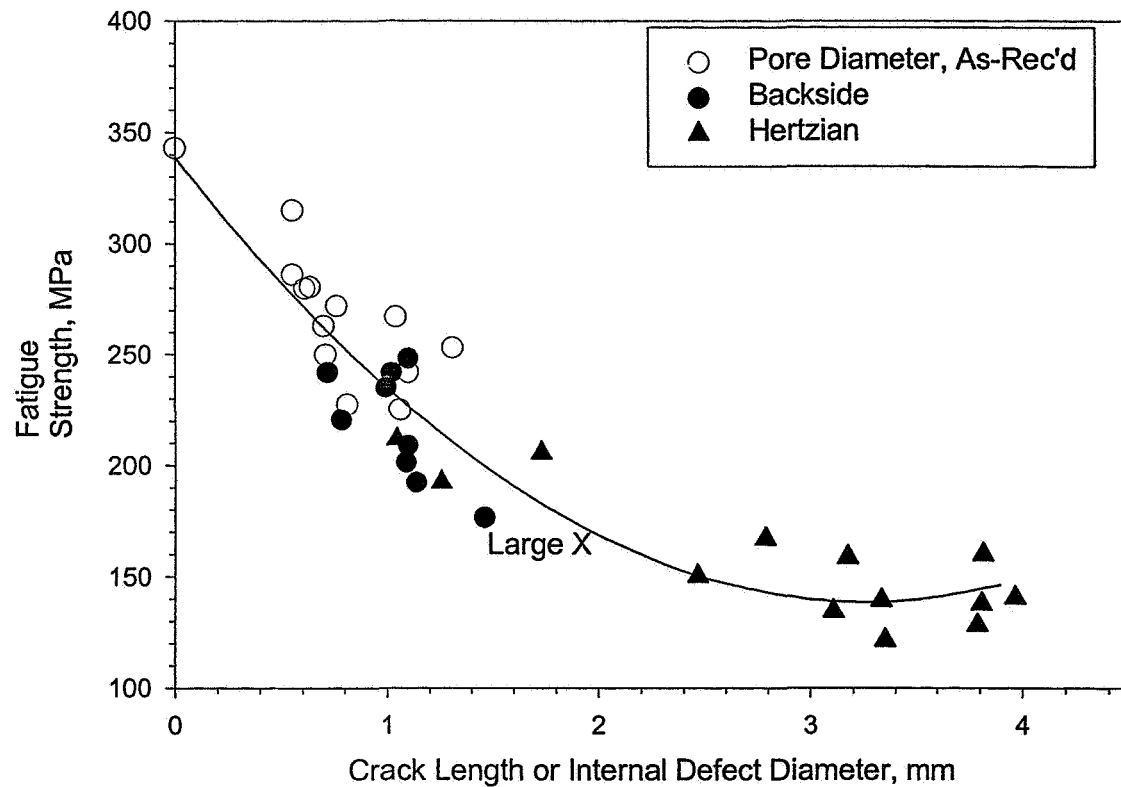


Figure 18. Fatigue strength was correlated to impact crack length or internal defect diameter for as-received samples. All data shown in this plot were generated at $R = 0.05$.

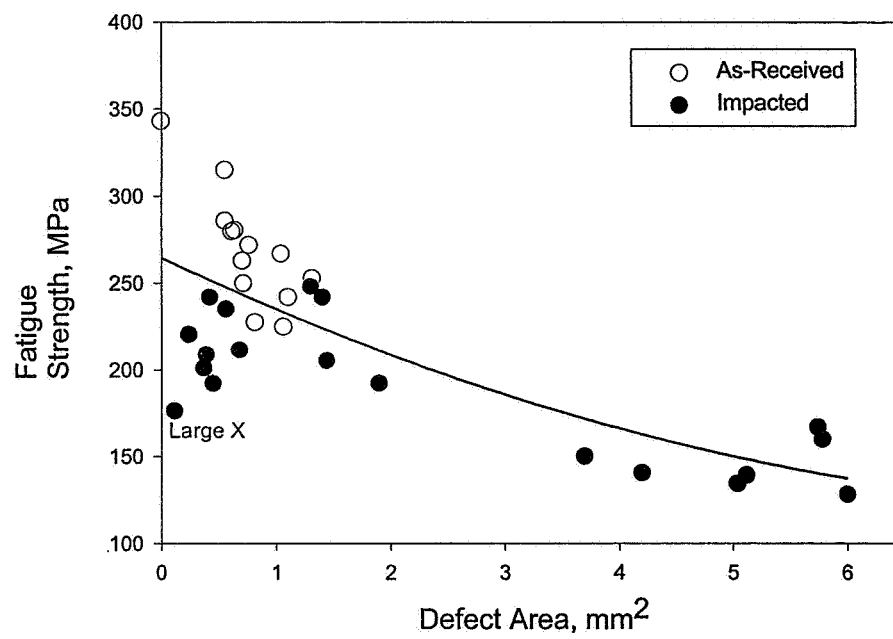
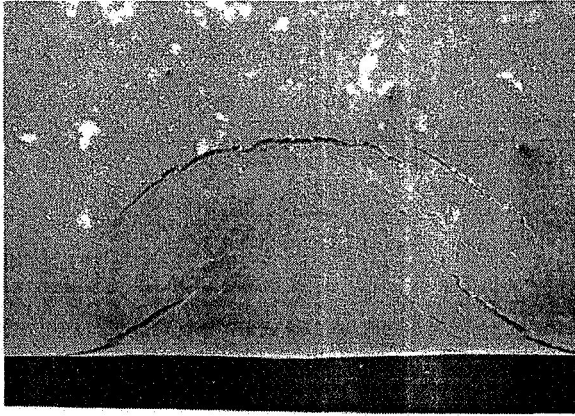
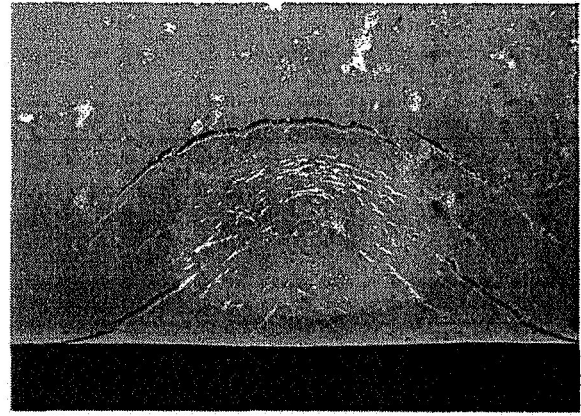


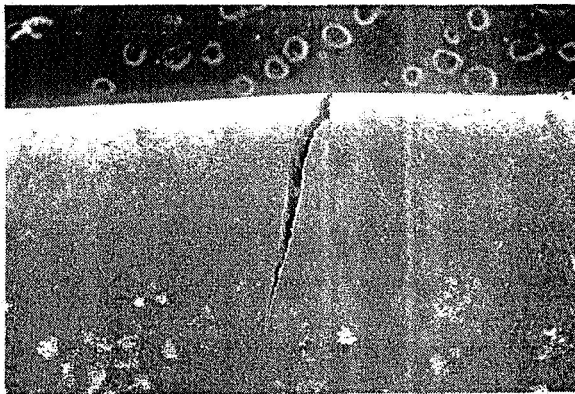
Figure 19. Effect of impact crack area or defect area on fatigue strength.



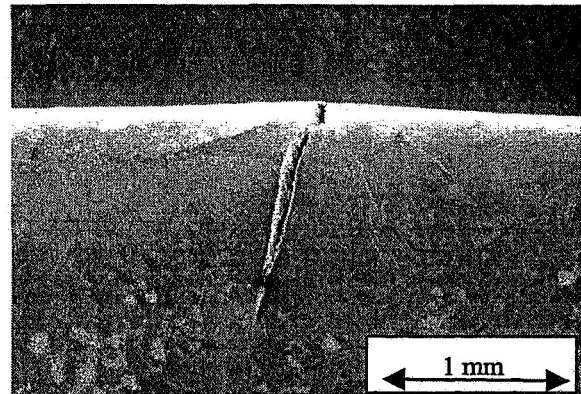
(a)



(b)



(c)



(d)

Figure 20. Surface cracks of a non-failure impact site did not propagate during fatigue testing. (a) Front and (c) backside of impact before fatigue testing, (b) front and (d) backside of impact after fatigue testing. Sample was impacted with 3.2 mm projectile at 1.05 J of energy. Fatigue failure initiated from a different impact site on the same specimen.

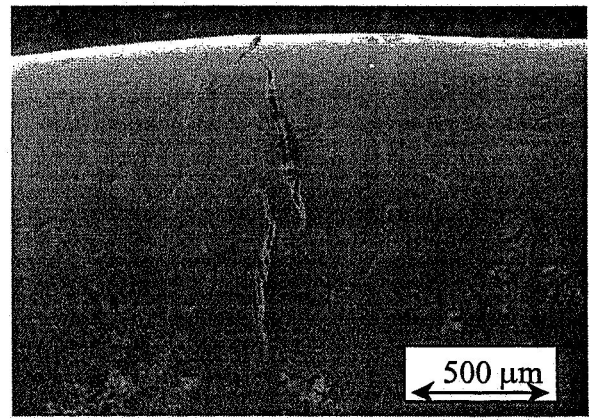
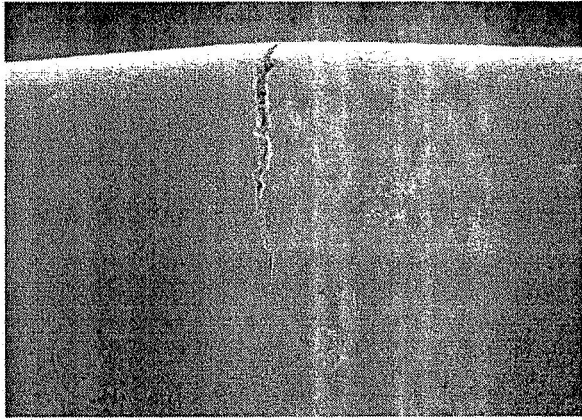


Figure 21. Wider, straighter backside crack of (a) initiated the fatigue failure of this sample instead of the longer but branched backside crack shown in (b).

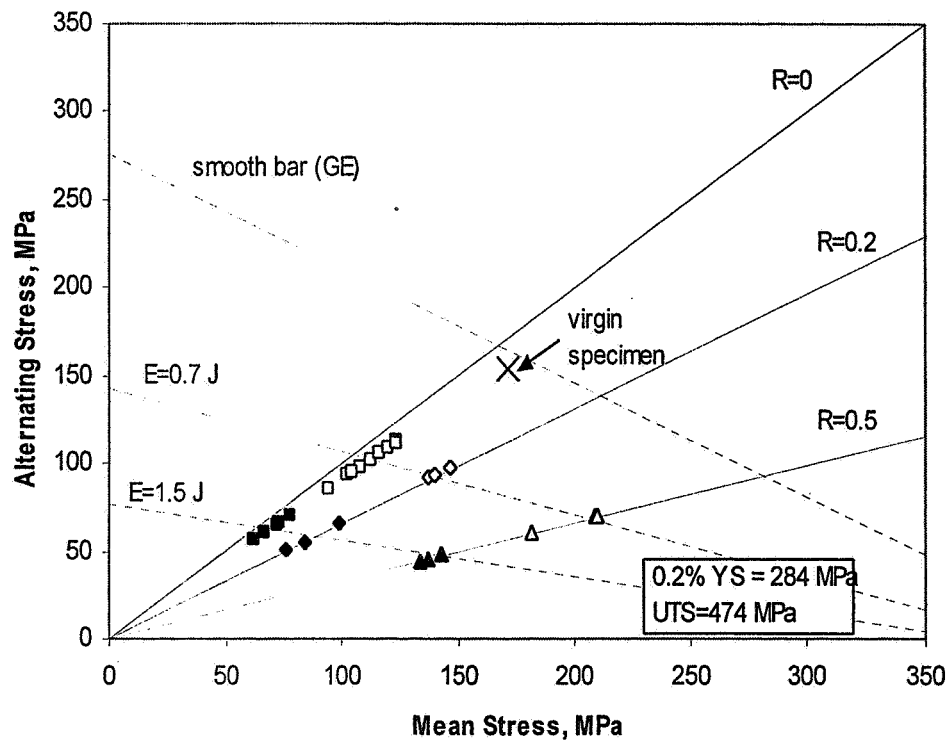


Figure 22. Goodman diagram for two impact energies, $E = 0.71 \text{ J}$ and $E = 1.52 \text{ J}$. Fatigue tests were run at 100 Hz and 650 °C.